A front-tracking method for computational modeling of viscoelastic two-phase flow systems

Daulet Izbassarov, Metin Muradoglu *

Department of Mechanical Engineering, Koç University, Rumelifeneri Yolu, 34450 Sariyer, Istanbul, Turkey

ABSTRACT

A front-tracking method is developed for direct numerical simulations of viscoelastic two-phase systems in which one or both phases could be viscoelastic. One set of governing equations is written for the whole computational domain and different phases are treated as a single fluid with variable material and rheological properties. The interface is tracked explicitly using a Lagrangian grid while the flow equations are solved on a fixed Eulerian grid. The surface tension is computed at the interface using the Lagrangian grid and included into the momentum equations as a body force. The Oldroyd-B, FENE-CR and FENE-MCR models are employed to model the viscoelasticity. The viscoelastic model equations are solved fully coupled with the flow equations within the front-tracking framework. A fifth-order WENO scheme is used to approximate the convective terms in the viscoelastic model equations and second-order central differences are used for all other spatial derivatives. A log-conformation method is employed to alleviate the high Weissenberg number problem (HWNP) and found to be stable and very robust for a wide range of Weissenberg numbers. The method has been first validated for various benchmark single-phase and two-phase viscoelastic flow problems. Then it has been applied to study motion and deformation of viscoelastic two-phase systems in a pressure-driven flow through a capillary tube with a sudden contraction and expansion. The method has been demonstrated to be grid convergent with second-order spatial accuracy for all the cases considered in this paper.

© 2015 Elsevier B.V. All rights reserved.

1. Introduction

Viscoelastic emulsions are ubiquitous in a wide range of engineering applications such as materials and food processing, pharmaceuticals, polymer blends and droplet-based microfluidics [51,49]. In particular, almost all the particle-laden biological fluids in nature exhibit viscoelastic behavior. Therefore it is of crucial importance to understand the dynamics of an individual viscoelastic droplet in a viscoelastic or Newtonian medium [51].

Computational modeling of viscoelastic fluid flow is a difficult task mainly due to the large disparity in time scales especially at high Weissenberg numbers known as the high Weissenberg number problem (HWNP). The existence of a moving and deforming interface in two-phase systems makes the problem even more complicated and challenging. Viscoelasticity has been usually modeled based on the microstructure of dilute polymer solutions and expressed by various constitutive differential equations such as upper convected Maxwell (UCM)/Oldroyd-B [40], Giesekus [22] and finitely extensible nonlinear elastic (FENE-P [5],

FENE-CR [13]) models for single and multiphase flow systems [51,42]. Various numerical approaches have been proposed to solve these models coupled with the flow equations. However the conventional numerical algorithms usually failed to converge above a certain Weissenberg number limit [42]. This stability problem is primarily caused by the exponential growth of viscoelastic stresses in regions of high shear rates or near stagnation points [42]. The failure of the numerical methods to properly approximate this exponential growth results in a numerical instability. Moreover this instability is pronounced if the positive definiteness of the conformation tensor is not preserved at the numerical solution level. The conformation tensor has a definite physical origin and interpretation stemming from the internal microstructure of polymer molecules in a continuum level [4] dictating the conformation tensor to be positive definite. Hulsen [26] proved that the conformation tensor must be initialized and remain positive definite for numerical stability. However, this condition can be violated in numerical approximations due to accumulation of numerical errors [42].

In a pioneering study, Keunings [28] observed failure of existing numerical methods at high Weissenberg numbers and attributed this failure to the inappropriate numerical methodologies. Since

* Corresponding author. Tel.: +90 (212) 338 14 73; fax: +90 (212) 338 15 48.
  E-mail address: mmuradoglu@ku.edu.tr (M. Muradoglu).

then, a number of stabilization approaches have been proposed to overcome the HWNP in viscoelastic flow simulations as recently discussed in details by Chen et al. [12]. Marchal and Crochet [31] developed one of the first successful numerical methods for simulations of viscoelastic flows at high Weissenberg numbers using upwind discretization of the convective terms in a mixed finite-element framework. Mompean and Deville [32] developed a finite-volume method and successfully performed simulations of Oldroyd-B fluid flow in a 3D planar contraction at high Weissenberg numbers. More recently, Fattal and Kupferman [20] developed the log-conformation method (LCM) based on reformulation of the constitutive equations using a logarithmic transformation of conformation tensor. The LCM has been shown to be stable and accurate at high Weissenberg numbers, i.e., as high as $Wi = 100$ [27]. This representation makes the problem more stable at numerical solution level since it preserves the positive definiteness of the conformation tensor and successfully captures sharp elastic stress layers. Sarkar and Schowalter [48] proposed a semi-analytical method (SAM) in which the exponential time variation is retained explicitly. In contrast with the LCM, the SAM does not require any eigen-decomposition so it has an advantage of having lower computation cost and implementation simplicity. However the positive definiteness of the conformation tensor is not preserved automatically in the SAM. Thus it may diverge at high Weissenberg numbers unless special treatments are done to guarantee the positive definiteness at numerical solution level. The SAM has been successfully used for two-phase viscoelastic flow simulations including shear [1,33] and buoyancy-driven [34] flows. However we found that, although the SAM is efficient at low or moderate Weissenberg numbers, it diverges when Weissenberg number exceeds a certain limit, i.e., $Wi > 2$, in simulating a viscoelastic droplet in a pressure-driven constricted channel. Therefore the SAM is used for low or moderate Weissenberg numbers while the LCM is employed at high Weissenberg numbers in the present study.

In spite of significant progress made for viscoelastic single-phase flow simulations, numerical methods have not yet reached maturity for simulating multiphase viscoelastic flows especially at high Weissenberg numbers. Tanner [50] performed a pioneering numerical study of die-swell problem using a Maxwell fluid model. Later Crochet and Keunings [19] simulated a circular and slit die-swell problem using the Oldroyd-B fluid model. Keunings and co-worker have also performed numerical simulations of various free-surface viscoelastic flows [9,10,28]. Kolte et al. [29] used a Lagrangian method to simulate the transient filament stretching rheometer. More recently various one-field formulations have been employed to perform direct numerical simulations of interfacial viscoelastic flows. Examples include the level-set [3,45], the volume of fluid (VOF) [14,23,25], marker and cell [43,53,54], phase-field [8,62,67], the conservative semi-Lagrangian advection scheme of constrained interpolation profile method with rational function (CIP-CSLR) [21] and the front-tracking methods [17,18,48]. In addition, versions of the arbitrary Lagrangian–Eulerian (ALE) [15,28,59,63,64] and the Lagrangian [47,61] methods have been also employed. Lind and Phillips [30] recently studied the effect of viscoelasticity on a rising gas bubble using a boundary element method. These methods have been used to investigate a wide range of interfacial viscoelastic flow problems including the jet buckling [6,39,54], extrudate swell [15,53,54], viscoelastic drop dynamics [17,18,33,43] and the cross-slot flow [43], among others.

The front-tracking method developed by Unverdi and Tryggvason [57] has been widely used to examine many aspects of Newtonian interfacial flows [55,36,52,37,41,38]. The method was extended to treat viscoelastic interfacial flows first by Sarkar

and Schowalter [48] and has been successfully used to study viscoelastic drop dynamics in shear and buoyancy-driven flows [1,33–35]. Sarkar and Schowalter [48] used the semi-analytical method that is limited to low or moderate Weissenberg numbers as mentioned earlier. Chung et al. [17,18] developed a finite-element/front-tracking method for simulation of viscoelastic interfacial flows in two-dimensional planar geometries using the log-conformation approach but the method is restricted to low Reynolds number (creeping) flows. This method has been successfully applied to study viscoelastic two-phase systems in a planar channel with a sudden constriction.

In the present study, a finite-difference/front-tracking method is developed for direct numerical simulation of viscoelastic two-phase flow systems including a Newtonian droplet in a viscoelastic medium (NV), a viscoelastic droplet in a Newtonian medium (VN) and a viscoelastic droplet in another viscoelastic medium (VV). Although the method is general and applicable to virtually any interfacial flow involving viscoelastic fluids, our main goal is to simulate the drop dynamics encountered or inspired by micro/bio-fluidic applications [52,58,65,66]. The method is designed to accommodate the generic family of viscoelastic model equations including the Oldroyd-B, FENE-CR of Chilcott Rallison [13] and FENE-MCR of Coates et al. [11]. The convective terms in viscoelastic constitutive equations are approximated using a second-order ENO [24] and fifth-order upwinded WENO-Z [7] schemes. It is found that the WENO-Z scheme outperforms the ENO scheme in resolving thin high viscoelastic stress layers near the interface. All the other spatial derivatives are approximated using central differences on a staggered grid. Both the semi-analytical and log-conformation methods are employed to overcome high Weissenberg number problem. It is found that the SAM is computationally more efficient than the LCM but fails to achieve convergence at high Weissenberg numbers especially for the pressure-driven viscoelastic two-phase flows in constricted capillary tubes. On the other hand, the LCM successfully achieves convergence for much higher Weissenberg numbers, e.g., as high as $Wi = 100$ without any difficulty but with a higher computational cost and increased implementation complexity. The method has been first validated for two benchmark single-phase problems. The first problem deals with the start-up Poiseuille flow of an Oldroyd-B fluid in a circular capillary tube. For this case, the numerical results are found to be in excellent agreement with the analytical solution obtained by Waters and King [60] both for the transient and steady state cases. The second benchmark problem concerns with a pressure-driven single-phase FENE-MCR fluid flow through an abrupt 4:1 constricted pipe. The results are compared and found to be in good agreement with the computational results of Coates et al. [11]. Then the method is applied to simulate the motion and deformation of a buoyancy-driven droplet in viscoelastic two-phase systems moving through a capillary tube studied computationally by You et al. [64]. The results are found to be in good agreement with You et al. [64] especially when the WENO-Z scheme is used to discretize the convective terms in the viscoelastic model equations. Finally the method has been successfully applied to a more challenging case involving motion and deformation of a droplet in pressure-driven viscoelastic two-phase systems flowing through a capillary tube with a sudden contraction and expansion. This test case holds a great promise to be a benchmark problem for testing performance of numerical methods developed to simulate viscoelastic two-phase systems of practical interest. The present numerical algorithm has been found to be very robust and grid convergent with second-order spatial accuracy for all the cases considered in this paper.

The main contributions of the present work can be summarized as follows:

1. The front-tracking method is extended for simulations of viscoelastic interfacial flows with significant inertial effects at high Weissenberg numbers using the log-conformation approach.

2. A fifth-order WENO-Z scheme is used for convective terms of the viscoelastic model equation, and found to be instrumental for resolving thin viscoelastic stress boundary layers especially near the interface. Note that the usual second-order central differences are unstable while second-order ENO schemes are excessively dissipative.

3. The method is general and applicable to two-phase systems in which phases can be all Newtonian, Newtonian-viscoelastic and viscoelastic–viscoelastic. It can accommodate virtually any viscoelastic model for each phase. Moreover, the method is readily extendible for simulation of multiphase systems in which more than two-phases may exist.

4. To the best of our knowledge, it is the first time that the front-tracking method is applied to pressure-driven viscoelastic interfacial flows in axisymmetic geometries with sudden contraction and expansion at finite Reynolds and Weissenberg numbers. The previous applications were restricted to 2D planar channels [17,18,25]. Moreover, simulations are performed for Newtonian-Newtonian, viscoelastic-Newtonian, Newtonian-viscoelastic and viscoelastic–viscoelastic cases.

The rest of this paper is organized as follows: In the next section, we briefly describe the governing equations including the constitutive models for viscoelasticity. The numerical method is presented in Section 3. The emphasis is placed on the numerical solution of viscoelastic model equations within the framework of the front-tracking method. The results are presented and discussed in Section 4. The method is first validated for single-phase and two-phase viscoelastic test problems, and then applied to viscoelastic two-phase systems in a pressure-driven flow through a circular pipe with a sudden contraction and expansion. Finally conclusions are drawn in Section 5.

2. Mathematical formulation

The governing equations are described in the context of the finite difference/front tracking method. The flow is assumed to be incompressible. Following Unverdi and Tryggvason [57], a single set of governing equations can be written for the entire computational domain provided that the jumps in the material properties such as density, viscosity and relaxation time are taken into account and the effects of the interfacial surface tension are treated appropriately.

The continuity and momentum equations can be written as follows:

$$\nabla \cdot \mathbf{u} = 0, \tag{1}$$

$$\frac{\partial \rho \mathbf{u}}{\partial t} + \nabla \cdot (\rho \mathbf{u}\mathbf{u}) = -\nabla p + \nabla \cdot \mu_s(\nabla \mathbf{u} + \nabla \mathbf{u}^T) + \nabla \cdot \boldsymbol{\tau} + \Delta\rho g$$
$$+ \int_A \sigma \kappa \mathbf{n} \delta(\mathbf{x} - \mathbf{x_f}) dA, \tag{2}$$

where $\mu_s, \rho, g, p, \mathbf{u}$ and $\boldsymbol{\tau}$ denote the solvent viscosity and the density of the fluid, the gravitational acceleration, the pressure, the velocity vector and the extra stress tensor, respectively. The last term in Eq. (2) represents the body force due to surface tension where σ is the surface tension coefficient, κ is twice the mean curvature, and $\mathbf{n}$ is the unit vector normal to the interface, respectively. The surface tension acts only on the interface as indicated by the three-dimensional delta function, δ, whose arguments $\mathbf{x}$ and $\mathbf{x_f}$

are the points at which the equation is evaluated and a point at the interface, respectively.

The Oldroyd-B, FENE-CR and FENE-MCR models are adopted as the constitutive equations for the viscoelastic extra stresses. These models can be written in a generic transport equation form as

$$\frac{\lambda}{F}\left(\frac{\partial \mathbf{E}}{\partial t} + \nabla \cdot (\mathbf{u}\mathbf{E}) - (\nabla \mathbf{u})^T \cdot \mathbf{E} - \mathbf{E} \cdot \nabla \mathbf{u}\right) + \mathbf{E} = \mathbf{S}, \tag{3}$$

where $\mathbf{E}$ can be extra stress or conformation tensor and $\mathbf{S}$ is a source term. In Eq. (3), $F, \mathbf{S}$ and $\boldsymbol{\tau}$ are specified in Table 1 for the three viscoelastic models considered in the present study. In this table, $\mu_p, \lambda, L, F, \mathbf{I}$ and $\boldsymbol{\tau}$ are the polymeric viscosity, the relaxation time, the ratio of the length of a fully extended polymer dumbbell to its equilibrium length, the stretch function, the identity and extra stress tensors, respectively. The conformation tensor is then defined as

$$\mathbf{A} = \frac{\lambda}{\mu_p F}\boldsymbol{\tau} + \mathbf{I}. \tag{4}$$

It is also assumed that the material properties remain constant following a fluid particle, i.e.,

$$\frac{D\rho}{Dt} = 0; \quad \frac{D\mu_s}{Dt} = 0; \quad \frac{D\mu_p}{Dt} = 0; \quad \frac{D\lambda}{Dt} = 0, \tag{5}$$

where $\frac{D}{Dt} = \frac{\partial}{\partial t} + \mathbf{u} \cdot \nabla$ is the material derivative. The density, polymeric and solvent viscosities, and the relaxation time vary discontinuously across the fluid interface and are given by

$$\mu_p = \mu_{p,i}I + \mu_{p,o}(1-I); \quad \mu_s = \mu_{s,i}I + \mu_{s,o}(1-I);$$
$$\rho = \rho_i I + \rho_o(1-I); \quad \lambda = \lambda_i I + \lambda_o(1-I), \tag{6}$$

where the subscripts i and o denote the properties of the drop and bulk fluids, respectively, and I is the indicator function defined such that it is unity inside the droplet and zero outside.

3. Numerical method

The viscoelastic flow equations are solved using the front-tracking method developed by Unverdi and Tryggvason [57]. This method is based on a single-field formulation of the flow equations for the entire computational domain and treats different phases as a single fluid with variable material properties. The emphasis is placed on describing the new ingredients and essential features of the method as it is applied to two-phase viscoelastic systems and specifically to the numerical solution of the viscoelastic model equations within the front-tracking framework.

3.1. Front-tracking method

The interface between different phases is represented by separate, non-stationary computational marker points connected to form a Lagrangian grid that lies within a stationary Eulerian grid as sketched in Fig. 1. The marker points move with the local flow velocity interpolated from the neighboring Eulerian grid points. Each piece of the interface between two neighboring marker points is called an interface (or front) element. The surface tension force is first computed at the centroids of the front elements using a

Table 1
Specification of the parameters $F, \mathbf{S}$ and $\boldsymbol{\tau}$ in Eq. (3).

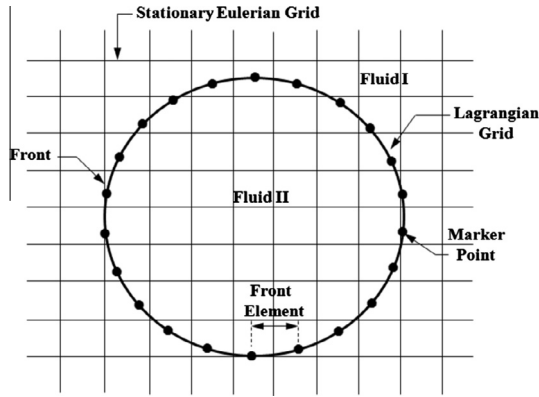| Model	F	$\mathbf{S}$	$\boldsymbol{\tau}$
Oldroyd-B	1	$\mathbf{I}$	$\mu_p F(\mathbf{E} - \mathbf{I})/\lambda$
FENE-CR	$L^2/(L^2 - \text{trace}(\mathbf{E}))$	$\mathbf{I}$	$\mu_p F(\mathbf{E} - \mathbf{I})/\lambda$
FENE-MCR	$(L^2 + \lambda\text{trace}(\mathbf{E})/\mu_p)/(L^2 - 3)$	$\mu_p(\nabla \mathbf{u} + \nabla \mathbf{u}^T)$	$\mathbf{E}$

Fig. 1. The Lagrangian and Eulerian grids used in computations. The flow equations are solved on the fixed Eulerian grid. The interface between different phases is represented by a Lagrangian grid consisting of connected marker points.

third-order Legendre polynomial fit through the end points of each element and the end points of the adjacent elements. These forces are then distributed on the neighboring staggered Eulerian grid points in a conservative manner and added to the discrete momentum equations as source terms in a similar way as discussed by Tryggvason et al. [55].

The front is also used to advect the discontinuous material property fields at each time step. First, the indicator function is computed. Based on the locations of the interface marker points, unit magnitude jumps are distributed in a conservative manner on the Eulerian grid points near the interface and are then integrated to obtain the indicator function everywhere. This procedure involves solution of a separable Poisson equation on the Eulerian grid and yields a smooth transition of the indicator function across the interface. Once the indicator function distribution is determined, the material properties are set as a function of the indicator function according to Eq. (6).

As the interface evolves, it greatly deforms and stretches. Thus some front elements become too large resulting in a lack of resolution while some become too small resulting in formation of wiggles much smaller than the grid size. To maintain accuracy, the Lagrangian grid is restructured at every time step by deleting the front elements that are smaller than a prespecified lower limit and by splitting the front elements that are larger than a prespecified upper limit to keep the front element size nearly uniform and comparable to the Eulerian grid size. The curvature of the interface is accounted for using a third-order Legendre polynomial fit in deleting and adding a front element as described by Tryggvason et al. [55].

Information must be passed between the Lagrangian and Eulerian grids at each time step since the locations of the marker points do not necessarily coincide with the stationary Eulerian grid points. This is achieved by approximating the infinitely thin interface by a smooth distribution function that is used to distribute the interfacial surface tension forces computed on the interface over the Eulerian grid points near the interface and also to interpolate the velocity onto the locations of the marker points from the Eulerian grid. Thus the front is given a finite thickness comparable to the mesh size in order to maintain stability and smoothness. This also prevents numerical diffusion since this thickness remains constant for all time. The Peskin's cosine distribution function [44] is employed for this purpose and found to perform well.

The details of the front-tracking method can be found in the original paper by Unverdi and Tryggvason [57], the review paper by Tryggvason et al. [55] and the recent book by Tryggvason et al. [56].

3.2. Flow solver

The flow equations are solved using a projection method on a staggered fixed Eulerian non-uniform Cartesian grid in which the velocity nodes are located at the cell faces while the material properties, the pressure and the extra stresses are all located at the cell centers. The spatial derivatives are approximated using central differences and time integration is performed using the projection method developed by Chorin [16]. Although a second-order accuracy in time can be easily achieved using a predictor–corrector scheme [55], a very conventional first order scheme is employed and briefly described here for completeness. In advancing solutions from time level n to level $n + 1$, first the interface is advanced for a time step using an explicit Euler method and the density field is updated based on the new locations of the marker points to obtain ρ^{n+1}. Then the momentum equation is integrated in two steps. In the first step, the pressure gradient is ignored and the unprojected velocity field is computed as

$$\frac{\rho^{n+1}\mathbf{u}^* - \rho^n\mathbf{u}^n}{\Delta t} = \left[-\nabla_h \cdot (\rho\mathbf{uu}) + \nabla_h \cdot (\mu_s(\nabla_h\mathbf{u} + \nabla_h^T\mathbf{u})) \right.$$
$$\left. + \Delta\rho g + \nabla\cdot\boldsymbol{\tau} + \int_A \sigma\kappa\mathbf{n}\delta(\mathbf{x} - \mathbf{x_f})dA \right]^n, \tag{7}$$

where Δt is the time step, ∇_h is the discrete version of the nabla operator and $\mathbf{u}^*$ is the unprojected velocity vector. In the second step, the velocity field is corrected as

$$\frac{\rho^{n+1}\mathbf{u}^{n+1} - \rho^{n+1}\mathbf{u}^*}{\Delta t} = -\nabla_h p^{n+1}. \tag{8}$$

Taking divergence of Eq. (8) and using the incompressiblity condition $\nabla_h \cdot \mathbf{u}^{n+1} = 0$, a non-separable Poisson equation is obtained for the pressure field in the form

$$\nabla_h \cdot \frac{1}{\rho^{n+1}}\nabla_h p^{n+1} = -\frac{1}{\Delta t}\nabla_h \cdot \mathbf{u}^*, \tag{9}$$

which is solved on the fixed Eulerian grid using a multigrid method as described by Tryggvason et al. [55].

3.3. Solution of the viscoelastic model equations

Numerical solution of the viscoelastic constitutive equations is notoriously difficult especially in two-phase systems mainly due to the large disparity in time scales and discontinuous variation of viscoelastic properties across the interfaces. To overcome these difficulties, two approaches are adopted in the present study. In the first approach, a semi-analytical method (SAM) developed by Sarkar and Schowalter [48] is used and found to be effective for Weissenberg numbers up to order of unity. For larger Weissenberg numbers, the log-conformation method (LCM) developed by Fattal and Kupferman [20] is employed.

In the SAM, the viscoelastic constitutive equations (e.g., Eq. (3)) are first written as

$$\frac{\lambda}{F}\frac{\partial\mathbf{E}}{\partial t} + \mathbf{E} = \mathbf{K}(t), \tag{10}$$

where

$$\mathbf{K}(t) = \mathbf{S} - \frac{\lambda}{F}\left[\nabla\cdot(\mathbf{uE}) - (\nabla\mathbf{u})^T\cdot\mathbf{E} - \mathbf{E}\cdot\nabla\mathbf{u}\right]. \tag{11}$$

Eq. (10) is integrated from time level n to level $n + 1$ for a time step Δt to get

$$\mathbf{E}^{n+1} = \mathbf{E}^n e^{-\Delta tF/\lambda} + \mathbf{K}^n(1 - e^{-\Delta tF/\lambda}), \tag{12}$$

where $\mathbf{K}$ and F are assumed to remain constant during the integration. This scheme is equivalent to an explicit Euler method as

$\Delta t \to 0$ and consistent everywhere (including the regions where $\lambda = 0$). The convective terms are approximated using a second-order ENO [24] or a fifth-order upwinded WENO-Z [7] scheme while central differences are used for all other spatial derivatives. In contrast with the LCM, the SAM does not automatically preserve positive definiteness of the conformation tensor. Thus the SAM becomes unstable at high Weissenberg numbers due to accumulation of numerical errors unless special treatments are done to ensure positive definiteness.

The LCM is used to overcome the well known high Weissenberg number problem (HWNP). In this approach, Eq. (3) is rewritten in terms of the logarithm of the conformation tensor through eigen-decomposition, i.e., $\boldsymbol{\Psi} = \log \mathbf{A}$. This representation ensures the positive definiteness of the conformation tensor. The core feature of the formulation is the decomposition of the gradient of divergence free velocity field $\nabla \mathbf{u}^T$ into two anti-symmetric tensors denoted by $\boldsymbol{\Omega}$ (pure rotation) and $\mathbf{N}$, and a symmetric tensor denoted by $\mathbf{C}$ which commutes with the conformation tensor [20], i.e.,

$$\nabla \mathbf{u}^T = \boldsymbol{\Omega} + \mathbf{C} + \mathbf{N} \mathbf{A}^{-1}. \tag{13}$$

Inserting Eq. (13) into Eq. (3) and replacing the conformation tensor with the new variable $\boldsymbol{\Psi}$, the transformed constitutive equations can be written as

$$\frac{\partial \boldsymbol{\Psi}}{\partial t} + \nabla \cdot (\mathbf{u} \boldsymbol{\Psi}) - (\boldsymbol{\Omega} \boldsymbol{\Psi} - \boldsymbol{\Psi} \boldsymbol{\Omega}) - 2\mathbf{C} = \frac{F}{\lambda}(e^{-\boldsymbol{\Psi}} - \mathbf{I}). \tag{14}$$

This equation is integrated using an explicit Euler scheme, i.e.,

$$\boldsymbol{\Psi}^{n+1} = \boldsymbol{\Psi}^n$$
$$+ \Delta t \left(-\nabla \cdot (\mathbf{u} \boldsymbol{\Psi}) + (\boldsymbol{\Omega} \boldsymbol{\Psi} - \boldsymbol{\Psi} \boldsymbol{\Omega}) + 2\mathbf{C} + \frac{F}{\lambda}(e^{-\boldsymbol{\Psi}} - \mathbf{I}) \right)^n, \tag{15}$$

where the spatial derivatives are again approximated using central differences except for the convective terms for which a second-order ENO [24] or a fifth-order upwinded WENO-Z [7] scheme is employed. The conformation tensor is then obtained using the inverse transformation as $\mathbf{A} = e^{\boldsymbol{\Psi}}$.

When the log-conformation method is used in the straightforward one-field formulation framework as described above, numerical difficulties arise at the viscoelastic/Newtonian interface since Eq. (15) becomes singular as $\lambda \to 0$ on the Newtonian side. To circumvent this problem, a simple procedure is employed here and found to be very robust. In this approach, the viscoelastic model equations are solved only in the viscoelastic region identified by the indicator function that is slightly truncated to avoid the singularity. For instance, the viscoelastic model equations are solved in the region where $I \geqslant \epsilon_I$ and $I \leqslant 1 - \epsilon_I$ for the VN and NV cases, respectively, and the viscoelastic stresses are set to zero otherwise. Since the viscoelastic stresses are zero in the Newtonian region, the conformation tensor equals to the identity tensor, (i.e., $\mathbf{A} = \mathbf{I}$) and $\boldsymbol{\Psi} = 0$ there. The cut off parameter ϵ_I is used to avoid the singularity on the Newtonian side and set to $\epsilon_I = 0.005$ in the present study. Note that the results are found to be insensitive to the value of the cut off parameter as long as $\epsilon_I < 0.01$.

4. Results and discussion

4.1. Single-phase flow

The method is first validated for viscoelastic single-phase flows. For this purpose, two test cases are considered. The first test case concerns with the start-up Poiseuille flow of an Oldroyd-B fluid in a circular pipe of radius R. The flow is assumed to be axisymmetric so a cylindrical coordinate system is adopted with z representing the axial direction aligned with the pipe axis and r the

radial direction. Waters and King [60] studied this problem and provided analytical solutions both for the transient and steady-state cases. Thus it serves an ideal test case for validation of the present numerical method. In this problem, the fluid is initially at rest and set into motion by a constant applied pressure gradient $G = -\frac{dp}{dz} = \text{const.}$ in the axial direction. No-slip and periodic boundary conditions are applied at the pipe wall and in the axial direction, respectively. Following dimensionless variables are introduced:

$$R^* = \frac{r}{R}; \quad T = \frac{t}{\lambda}; \quad V = \frac{v_z}{v_0}; \quad \beta = \frac{\mu_s}{\mu_0}; \quad Re = \frac{\rho v_0 R}{\mu_0}; \quad Wi = \frac{\lambda v_0}{R}, \tag{16}$$

where v_z is the axial velocity and $\mu_0 = \mu_s + \mu_p$ is the total viscosity. In Eq. (16), the velocity scale v_0 is defined as $v_0 = -\frac{R^2}{8\mu_0}\frac{dp}{dz}$. Computations are performed on a uniform grid with grid size $\Delta r = R/128$ for three different Weissenberg numbers, i.e., $Wi = 1, 10$ and 100. The other dimensionless parameters are kept constant at $Re = 1$ and $\beta = 0.1$. Fig. 2a shows the velocity profiles at various dimensionless times for $Wi = 10$. The evolution of the centerline velocity is plotted in Fig. 2b for $Wi = 1, 10$ and 100. As can be seen in these figures, there is excellent agreement between the computational and analytical results indicating the accurate solution of the viscoelastic model equations. Note that, although not shown here due to space consideration, the steady state results of the viscoelastic stresses and velocity are also found to be in good agreement with the analytical solutions.

The second test case deals with a single-phase viscoelastic fluid flow through an abrupt axisymmetric 4:1 contraction. This flow has been widely used as a benchmark problem for validation of computational methods, see e.g., Owens and Phillips [42]. The FENE-MCR model is employed here to facilitate comparison of the present results with Coates et al. [11]. The semi-analytical method is used for this test problem. The channel consists of two circular tubes. The fluid passes from the larger channel of radius R_1 into the narrower channel of radius R_2. The relevant dimensionless parameters are the viscosity ratio $\beta = \mu_s/\mu_0$, the Reynolds number $Re = \rho U R_2/\mu_0$ and the Weissenberg number $Wi = \lambda U/R_2$, where $\mu_0 = \mu_s + \mu_p$ is the total viscosity and U is the average velocity in the narrow channel. The present results are compared with the computational simulations of Coates et al. [11]. For this purpose, the streamline patterns are shown in Fig. 3 in the vicinity of the constriction for two different Weissenberg numbers. As can be seen in the figure, the present results are overall in good agreement with those of Coates et al. [11], i.e., the vortex stretches towards the reentrant corner and grows in upstream direction with increasing Weissenberg number and the vortex lengths compare well in both simulations. Although not included in the paper, there is also good quantitative agreement between the present simulations and the results of Coates et al. [11] for all flow quantities including the mean velocity and the extra stress components.

4.2. Multiphase flow

After validating the numerical algorithm for the benchmark single-phase viscoelastic flows, the method is now applied to study two-phase viscoelastic flow systems. For this purpose, the method is first validated for the buoyancy-driven viscoelastic droplet systems studied computationally by You et al. [64]. Then the performance of the numerical method is demonstrated for a more challenging two-phase viscoelastic flow system involving the motion and deformation of a droplet in a pressure-driven constricted channel.
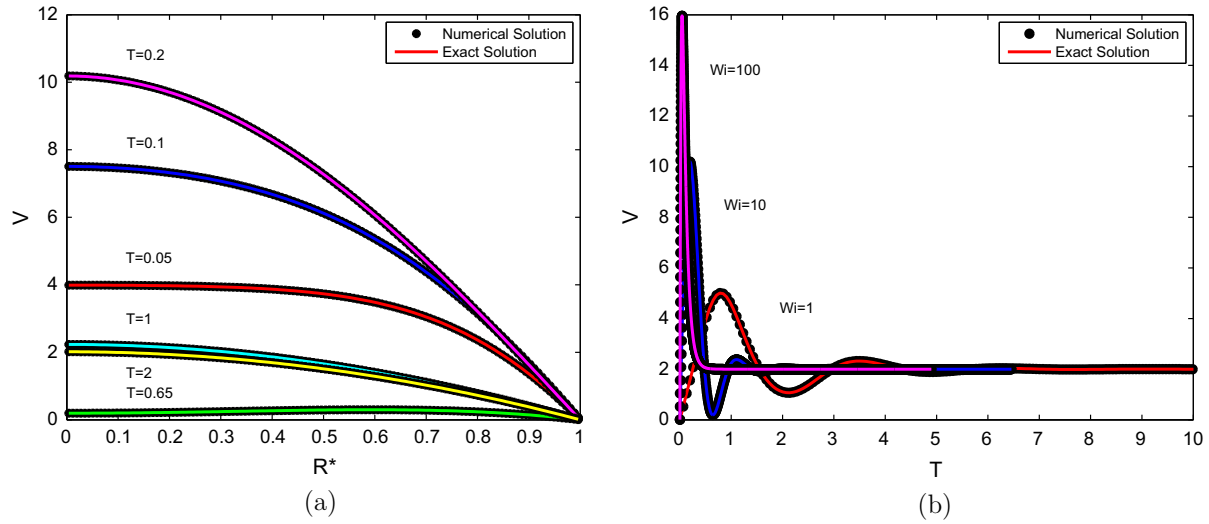
Fig. 2. The start-up Poiseuille flow: (a) The velocity profiles at different non-dimensional times for $Wi = 10$. (b) The evolution of centerline velocity for $Wi = 1, 10$ and 100. The symbols represent the computational results and the solid lines are the analytical solution of Waters and King [60].
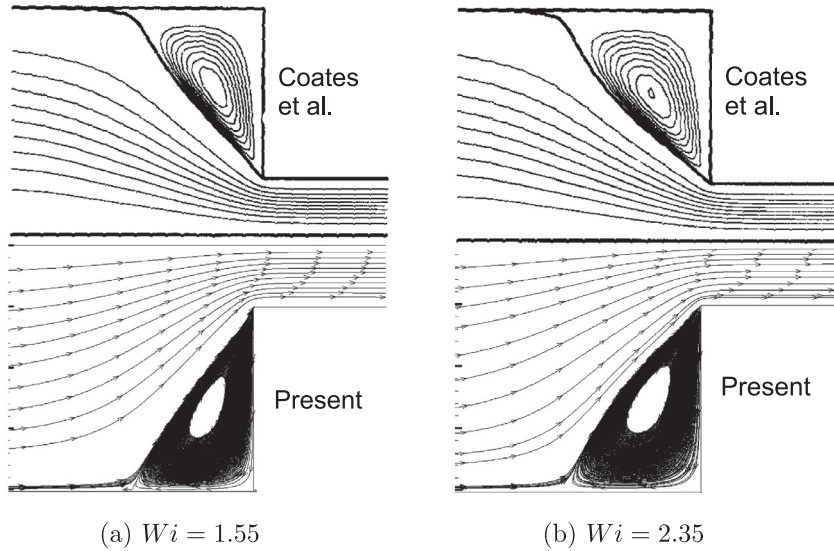

(a) $Wi = 1.55$ (b) $Wi = 2.35$

Fig. 3. The vortices computed in the corner of the 4:1 contraction using the FENE-MCR model. (a) $Wi = 1.55$ and (b) $Wi = 2.35$. The present results (bottom portion) are compared with the results of Coates et al. [11] (top portion). ($Re = 0.1, \beta = 0.01$, and $Grid : 128 \times 320$).

4.2.1. Buoyancy-driven viscoelastic two-phase systems in a capillary tube

You et al. [64] considered buoyancy-driven droplet systems in which either the droplet or the bulk fluid could be viscoelastic. In addition to these two flow systems, we also consider the case in which both the phases are viscoelastic with different rheological properties. The FENE-CR model is employed in the present simulations to facilitate direct comparison with the results of You et al. [64]. The physical problem is shown schematically in Fig. 4. The tube has a diameter of $1.4d_d$ and a length of $6.5d_d$, and are closed at both ends. A spherical droplet of diameter d_d is initially located at the centerline of the tube with a $1.5d_d$ distance from the bottom wall. Flow is assumed to be axisymmetric and no-slip boundary conditions are applied at the walls. For the conformation tensor, the Neumann and axisymmetric boundary conditions are applied on the walls and at the centerline, respectively. The droplet starts moving due to buoyancy from rest in an otherwise quiescent ambient fluid. Following You et al. [64], the non-dimensional parameters are defined as follows:

$$Re = \frac{\rho V^* d_d}{\mu_s}; \quad Ca = \frac{\mu_s V^*}{\sigma}; \quad Wi = \frac{\lambda V^*}{d_d};$$

$$\theta = \frac{\mu_{s,i}}{\mu_{s,o}}; \quad \alpha = \frac{\rho_i}{\rho_o}; \quad k = \frac{\lambda_i}{\lambda_o}, \tag{17}$$

where Re, Ca, and Wi represent the Reynolds, capillary and Weissenberg numbers, respectively. In Eq. (17), the velocity scale is defined as $V^* = (\rho_o - \rho_i)g d_d^2/\mu_s$ where g is the gravitational acceleration. The other parameters θ, α and k denote the solvent viscosity, the density and the relaxation time ratios, respectively. Unless specified otherwise, the viscosity and density ratios are fixed at $\theta = 0.5, \beta = 0.77$, and $\alpha = 0.5$ for the results presented in this section. The computations are performed using dimensional quantities but the results are made dimensionless with the length scale d_d and time scale $t^* = d_d/V^*$. Note that You et al. [64] defined a slightly different conformation tensor that is related to **A** as **B** = **A** − **I**.

Extensive computations are performed to examine the effects of the viscoelasticity on drop mobility and deformation. The viscoelastic constitutive equations are solved using the
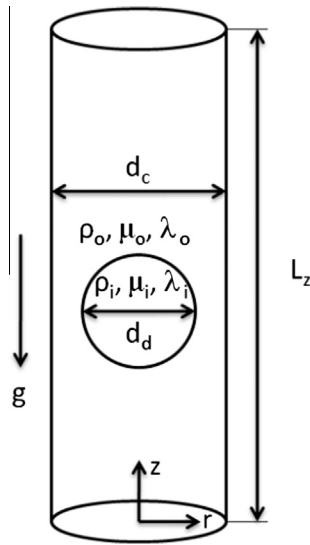
Fig. 4. Schematic illustration of a buoyancy-driven viscoelastic two-phase system.

semi-analytical method. The computational domain is resolved by a 128 × 1184 grid. The constant contours of the components of the conformation tensor are plotted in Figs. 5 and 6 in the vicinity of the droplet in a steady motion for a viscoelastic droplet in a Newtonian medium (VN) and a Newtonian droplet in a viscoelastic medium (NV), respectively, together with the computational results of You et al. [64]. These figures show that a Newtonian drop immersed in a viscoelastic fluid experiences an extending trailing edge while a viscoelastic drop in a Newtonian fluid develops an indentation around the rear stagnation point. Moreover, in both cases, there is a thin layer at the interface in the leading and trailing edges of the droplet where the viscoelastic stress concentration occurs with a sharp gradient due to large polymer extensions. These results are overall in good qualitative and quantitative agreement with the computational simulations of You et al. [64]. The slight difference in the maximum magnitudes of some components of the conformation tensor between the present results and the results of You et al. [64] is mainly attributed to the lack of resolution of the thin viscoelastic layer at the interface in the present simulations. Note that You et al. [64] used a separate body-fitted curvilinear grid for each phase. Therefore they were able to greatly stretch the grids near the interface resulting in a good resolution of the thin viscoelastic layers there for these particular flow systems. The terminal velocities of the VN and NV systems are shown in Fig. 7 where the steady drop shapes are also plotted. The terminal velocity is slightly under predicted for the VN system while it is over predicted for the NV system. However, the steady drop shapes are in good agreement with those of You et al. [64]. Further simulations are also performed to examine dynamics of a buoyancy-driven viscoelastic droplet immersed in another viscoelastic medium for a wide range of elasticity ratio $k = \lambda_i/\lambda_o$. Two sample results are shown in Fig. 8 for $k = 0.2$ and $k = 5$ to demonstrate the ability of the present method for simulation of vis
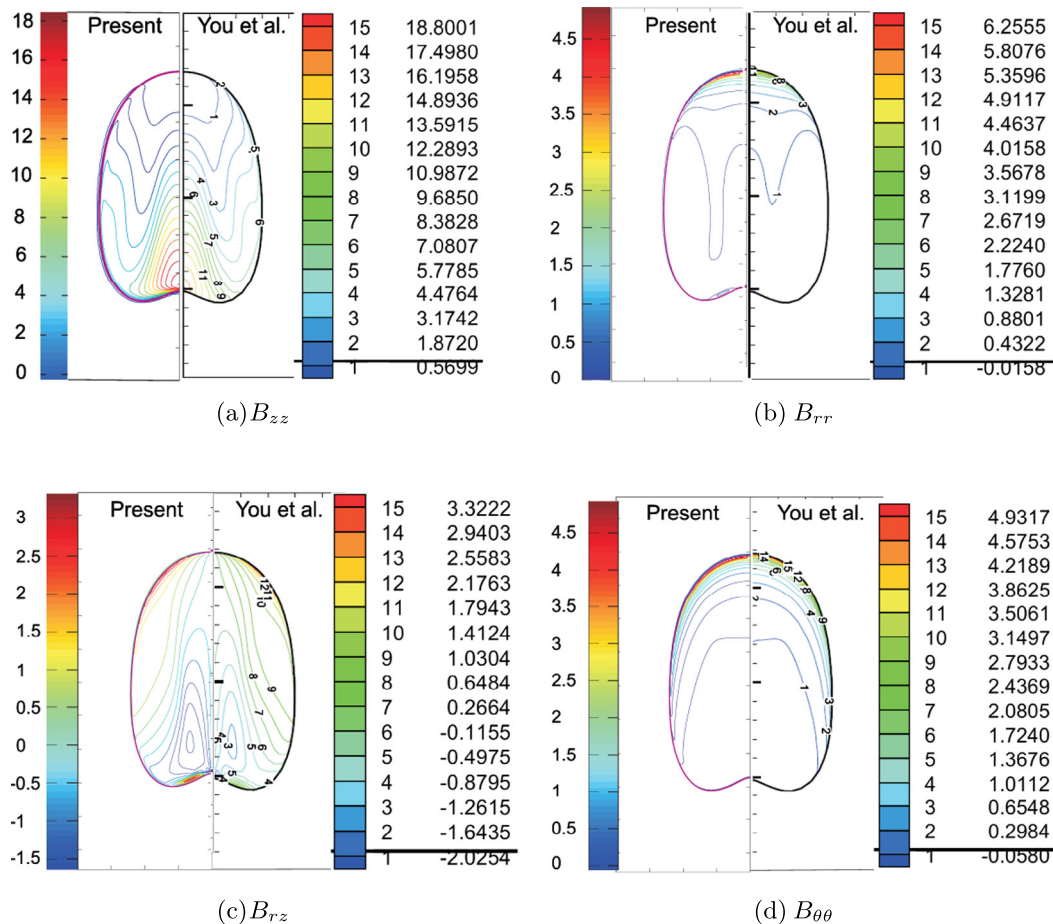

(a) B_{zz}

(b) B_{rr}

(c) B_{rz}

(d) $B_{\theta\theta}$

Fig. 5. The steady droplet shapes and the constant contours of the conformation tensor **B** for a buoyancy-driven FENE-CR droplet rising in a Newtonian fluid. The present results (left portion) are compared with the results of You et al. [64] (right portion). ($Re = 10, Ca = 50, Wi = 50, Grid : 128 \times 1184$).
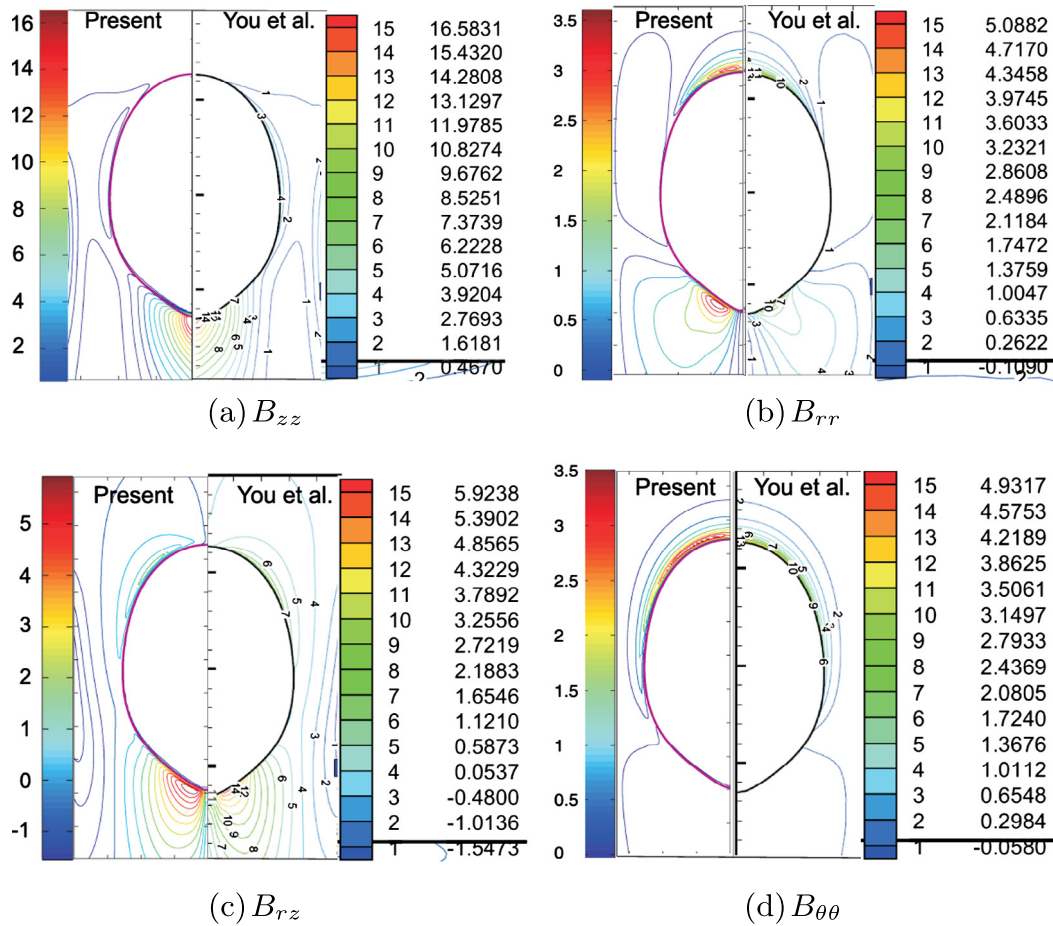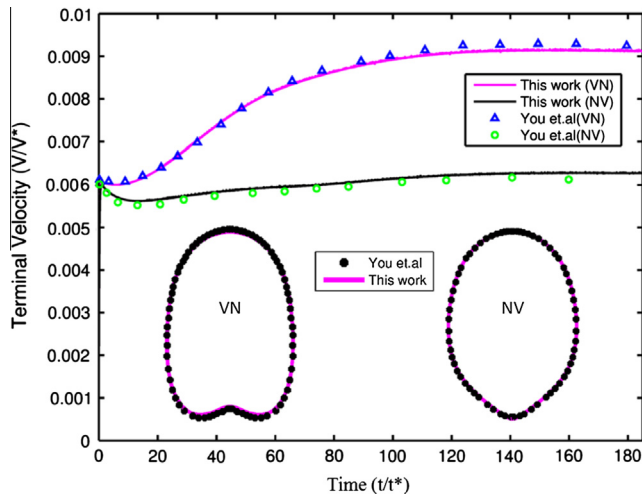
(a) B_{zz}

(b) B_{rr}

(c) B_{rz}

(d) $B_{\theta\theta}$

Fig. 6. The steady droplet shapes and the constant contours of the conformation tensor **B** for a buoyancy-driven Newtonian droplet rising in a FENE-CR fluid. The present results (left portion) are compared with the results of You et al. [64] (right portion). ($Re = 10, Ca = 20, Wi = 50, Grid : 128 \times 1184$).

Fig. 7. The terminal velocity versus the non-dimensional time for a droplet in the VN and NV systems, and their respective steady shapes. Solid lines are the present results and the symbols are the results of You et al. [64]. The results are obtained using a 128×1184 grid. (VN case: $Re = 10, Ca = 50, Wi = 50$; NV case: $Re = 10, Ca = 10, Wi = 100$).

coelastic–viscoelastic two-phase systems. As can be seen in this figure, $k = 0.2$ case resembles the NV system while $k = 5$ resembles the VN system.

The properties of the numerical algorithm are also examined for this test case. For this purpose, first the second-order ENO and the

fifth-order upwinded WENO-Z schemes are compared for the VN and NV systems in Fig. 9. Considering the results of You et al. [64] shown in Figs. 5 and 6, Fig. 9 clearly demonstrates that the WENO-Z scheme outperforms the ENO scheme in resolving the thin viscoelastic layer at the interface. The WENO-Z scheme is particularly successful for the VN case providing a comparable resolution with the results of You et al. [64] whereas the ENO scheme results in about 40% under prediction in terms of the maximum magnitude of $B_{\theta\theta}$ and B_{rr} on the same grid. It is also emphasized here that the extra stress boundary conditions are more easily implemented for the VN case since the viscoelasticity is essentially confined in the flow domain far from the tube walls. Then the consistency of the semi-analytical and log-conformation methods is examined. The semi-analytical and log conformation methods are mathematically identical so they must be consistent at the numerical solution level within the spatial and temporal discretization errors. This is verified in Fig. 10 where the constant contours of $B_{\theta\theta}$ and B_{zz} obtained by the two methods are compared. As can be seen from this figure, both methods yield essentially the same results indicating good consistency of two approaches. We also note that, although not shown here, both methods have been comprehensively compared for a wide range of flow conditions and found to be in excellent agreement for all the cases. It is worth stressing that no HWNP related instability has been observed for this buoyancy-driven flow case when the SAM is employed even for very high Weissenberg numbers, i.e., as high as $Wi = 1000$.

It is well known that the vanishing solvent viscosity poses a significant challenge for most numerical methods and often leads to
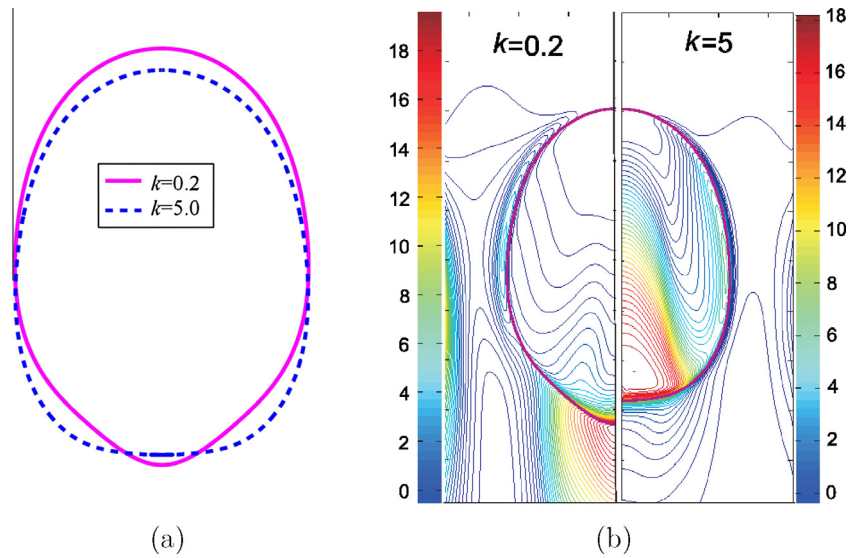
Fig. 8. A buoyancy-driven FENE-CR droplet rising in another FENE-CR fluid for $k = 0.2$, $Wi_i = 20$ and $Wi_o = 100$ and for $k = 5$, $Wi_i = 100$ and $Wi_o = 20$. (a) The steady shapes, and (b) the constant contours of the conformation tensor component B_{zz}. ($Re = 10$, $Ca = 20$, $Grid : 64 \times 592$).
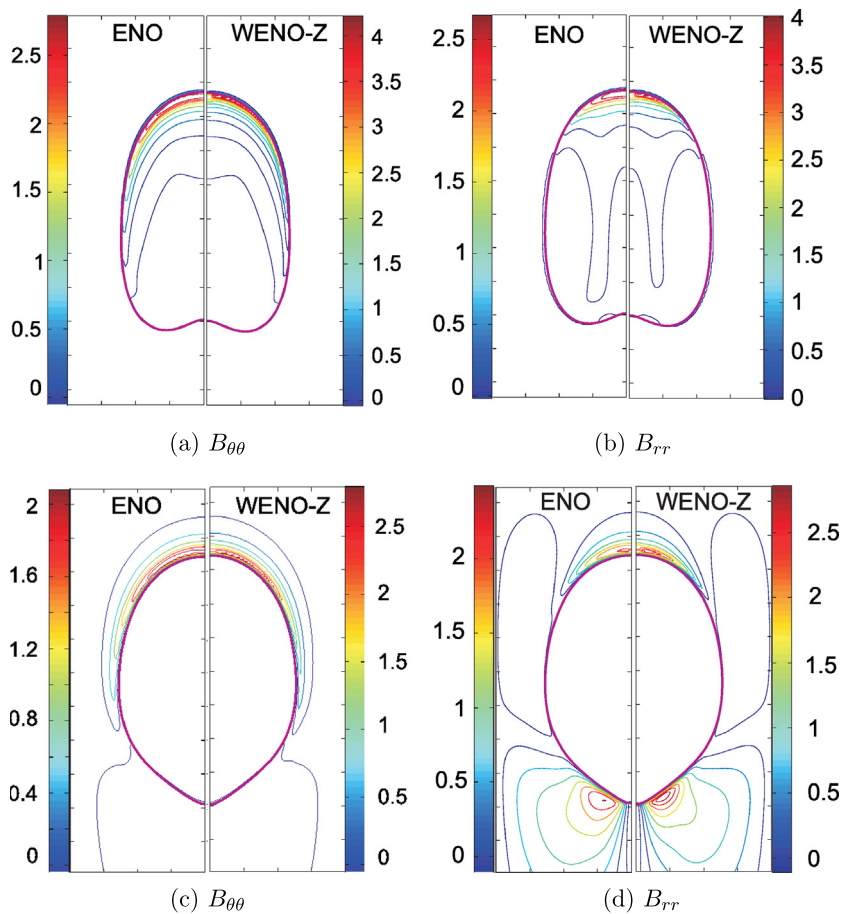

Fig. 9. The second-order ENO versus the fifth-order upwinded WENO-Z schemes. The constant contours of the conformation tensor components $B_{\theta\theta}$ and B_{rr} for VN and NV cases. (VN case: $Re = 10$, $Ca = 50$, $Wi = 50$; NV case: $Re = 10$, $Ca = 20$ and $Wi = 50$; $Grid : 64 \times 592$).

numerical instabilities [2] mainly due to the loss of the elliptic nature of the governing equations as $\mu_s \to 0$. The performance of the present numerical method is examined through extensive simulations for a range of solvent viscosity ratios (β) while keeping the other parameters fixed. For this purpose, the solvent viscosity ratio

is varied in the range $\beta = 0.1$ and $\beta = 10^{-4}$ by successively increasing the polymeric viscosity and reducing solvent viscosity such that the total viscosity remains the same. The steady drop shapes and corresponding constant contours of trace(**B**) are shown in Figs. 11 and 12 for the VN and NV systems, respectively. Note that
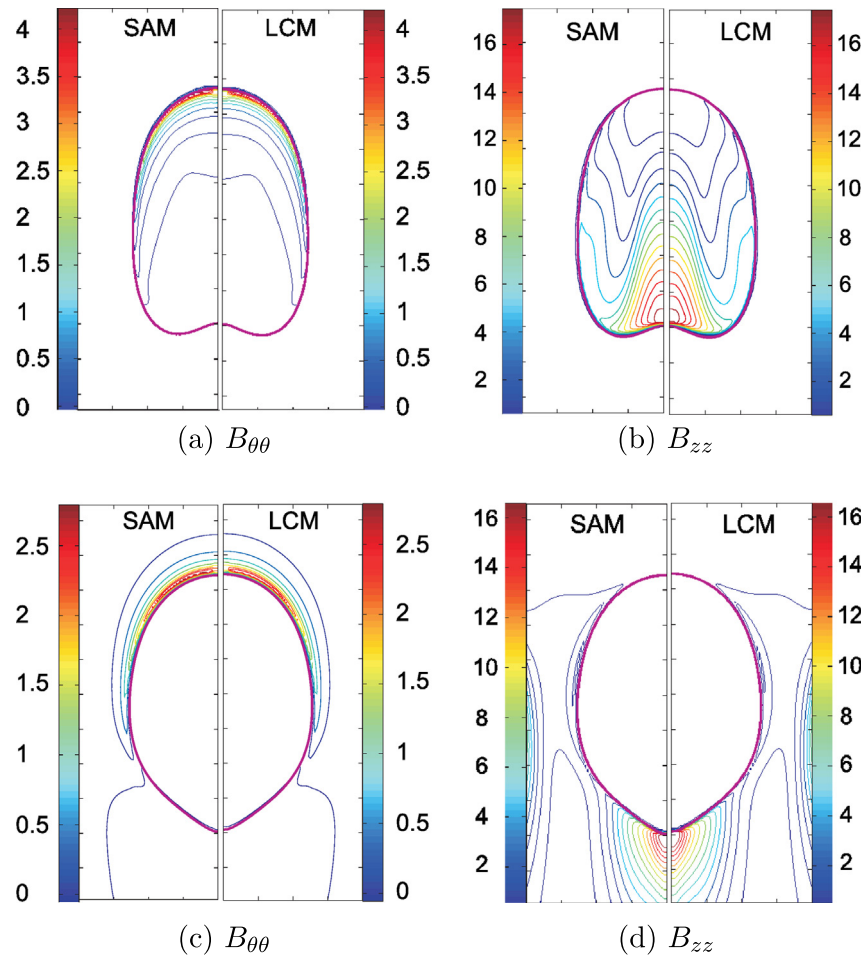
Fig. 10. The semi-analytical method (SAM) versus the log-conformation method (LCM). The constant contours of the conformation tensor components $B_{\theta\theta}$ and B_{zz} for VN and NV cases. (VN case: $Re = 10, Ca = 50, Wi = 50$; NV case: $Re = 10, Ca = 20$ and $Wi = 50; Grid : 64 \times 592$).

the results for $\beta = 10^{-4}$ case are not shown in Figs. 11 and 12 since the effects of β become negligible after $\beta < 0.01$ and thus the results of $\beta = 10^{-3}$ and $\beta = 10^{-4}$ cases are indistinguishable for both NV and VN cases. It is found that the present method remains very robust even for $\beta = 10^{-4}$ case without any sign of instability. As β decreases, the viscoelastic stresses grow and can dominate over the surface tension. In the VN case, when β is reduced below a threshold value, the surface tension cannot balance the viscoelastic stresses anymore and the dimple created at the trailing edge penetrates through the droplet and eventually forms a toroidal shape as seen in Fig. 11. Similar drop deformation was also observed by Mukherjee and Sarkar [34] for a viscoelastic drop falling through a viscous medium. It is also interesting to observe that the droplet mobility increases and the terminal velocity becomes more oscillatory for smaller β values as shown in Fig. 13. These results are consistent with the results of Pillapakkam et al. [46] and Lind and Phillips [30]. We finally note that, in the NV case, the increased viscoelastic stresses sharpen the trailing edge of the droplet as β decreases as seen in Fig. 12.

Finally the spatial and temporal accuracy of the numerical method is examined for the VN case. In the present method, the numerical error can be generally decomposed into spatial and time-stepping errors. First, computations are performed using various grid resolutions ranging between 32×296 and 128×1184 to show the overall dependence of the numerical results on grid refinement. The terminal velocity is plotted against the

non-dimensional time in Fig. 14a while trace(**B**) is computed at the drop centerline and plotted against the local vertical position of drop measured from the trailing edge in Fig. 15a. As can be seen in these figures, differences between successive grid resolutions decrease as grid is refined indicating grid convergence. Furthermore, the terminal velocity and trace(**B**) are plotted in Figs. 14b and 15b, respectively, as a function of square of non-dimensional grid size. The approximate linear relation indicates expected second-order spatial accuracy of the method. Fig. 14b also shows that a 64×592 grid is sufficient to reduce the maximum spatial error in terminal velocity below 1%. However, much finer grid is required to resolve the thin viscoelastic stress boundary layer near the interface. For instance, even the finest grid can reduce the spatial error only below 4% for trace(**B**) at the leading edge stagnation point.

Since the present numerical method is explicit, the time step is strictly restricted by the stability conditions so the time stepping error is expected to be small compared to the spatial error. To check this, simulations are performed for various time steps using a 64×592 grid. The results are shown in Fig. 16 where the non-dimensional axial coordinate of droplet centroid is plotted against the non-dimensional time (Fig. 16a) and trace(**B**) is plotted along the droplet centerline in steady motion (Fig. 16b) for various time steps. As can be seen in this figure, the temporal error is negligible even for the maximum time step allowed by the stability constraints.
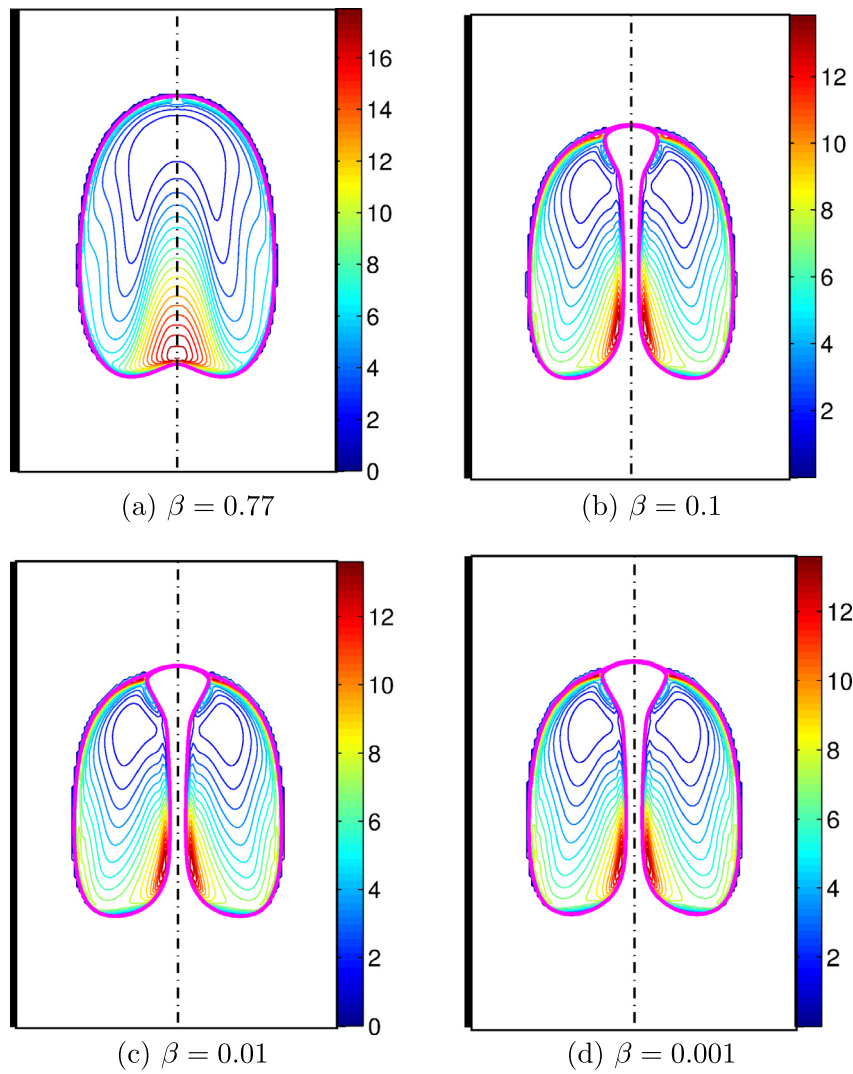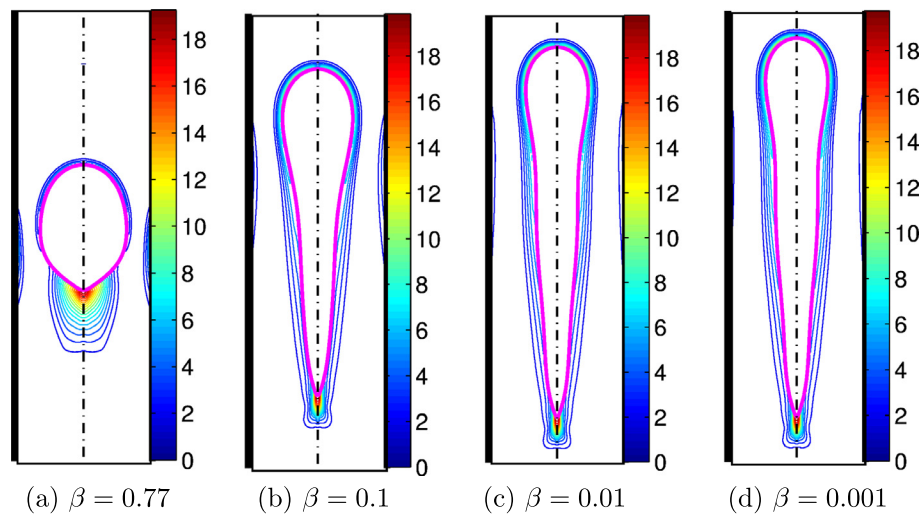
Fig. 11. The effects of solvent viscosity ratio (β) for the VN case. The steady droplet shapes are shown together with the constant contours of trace(**B**) for a buoyancy-driven FENE-CR droplet rising in a Newtonian fluid. ($Re = 10, Ca = 50, Wi = 50, Grid : 64 \times 592$).

Fig. 12. The effects of solvent viscosity ratio (β) for the NV case. The steady droplet shapes are shown together with the constant contours of trace(**B**) for a buoyancy-driven Newtonian droplet rising in a FENE-CR fluid. ($Re = 10, Ca = 20, Wi = 50, Grid : 64 \times 592$).
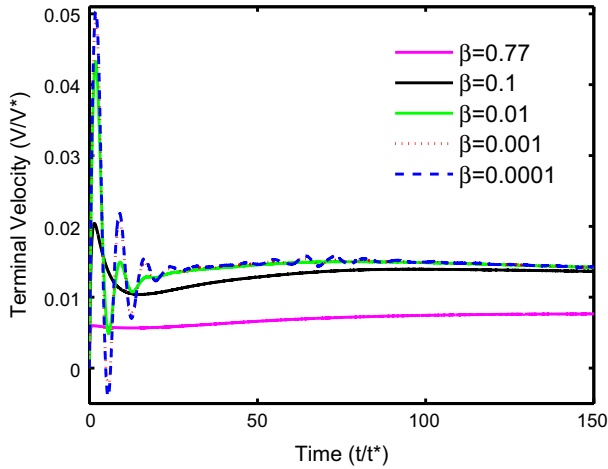
Fig. 13. The effects of solvent viscosity ratio (β) for the NV case. The terminal velocity is plotted against the non-dimensional time for various β ranging between $\beta = 0.77$ and $\beta = 0.0001$. ($Re = 10, Ca = 10, Wi = 100, Grid : 64 \times 592$.)
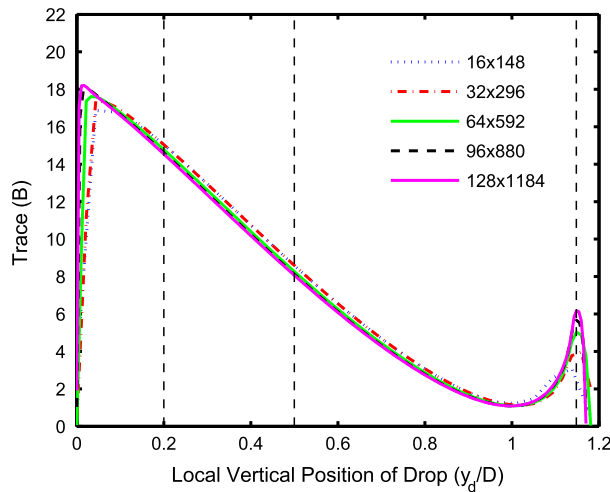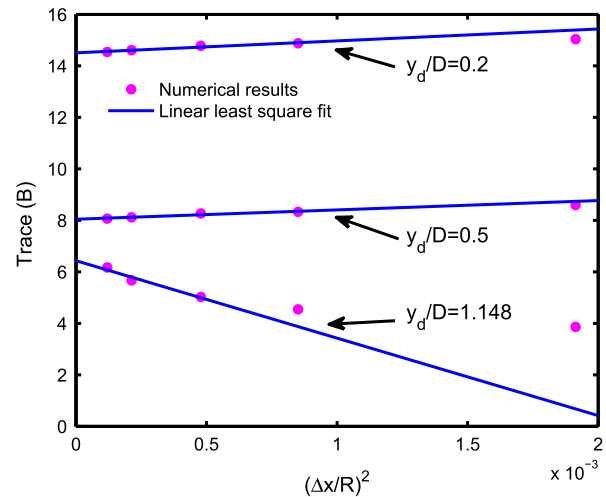
4.2.2. Pressure-driven viscoelastic two-phase systems in a capillary tube with sudden contraction and expansion

The method is finally applied to study the viscoelastic two-phase systems in a capillary tube with a sudden contraction and expansion. A viscoelastic droplet in a Newtonian medium (VN), a Newtonian droplet in a viscoelastic medium (NV) and a viscoelastic droplet in another viscoelastic medium (VV) cases are considered. In addition to the well known stress singularities at the corners of the constriction, the strong droplet-constriction interactions and the subsequent large droplet deformations pose a challenge for the numerical solution algorithms. In particular, when a large droplet is forced to squeeze through the constriction at low capillary and high Weissenberg numbers, it undergoes large deformations leading to significant viscoelastic stress build ups especially near the corners of the constriction. It is worth mentioning here that the Oldroyd-B model is used for this test case in order to demonstrate the robustness of the present numerical method since the numerical solution of Oldroyd-B model equations is generally deemed to be more difficult than that of the FENE type models.
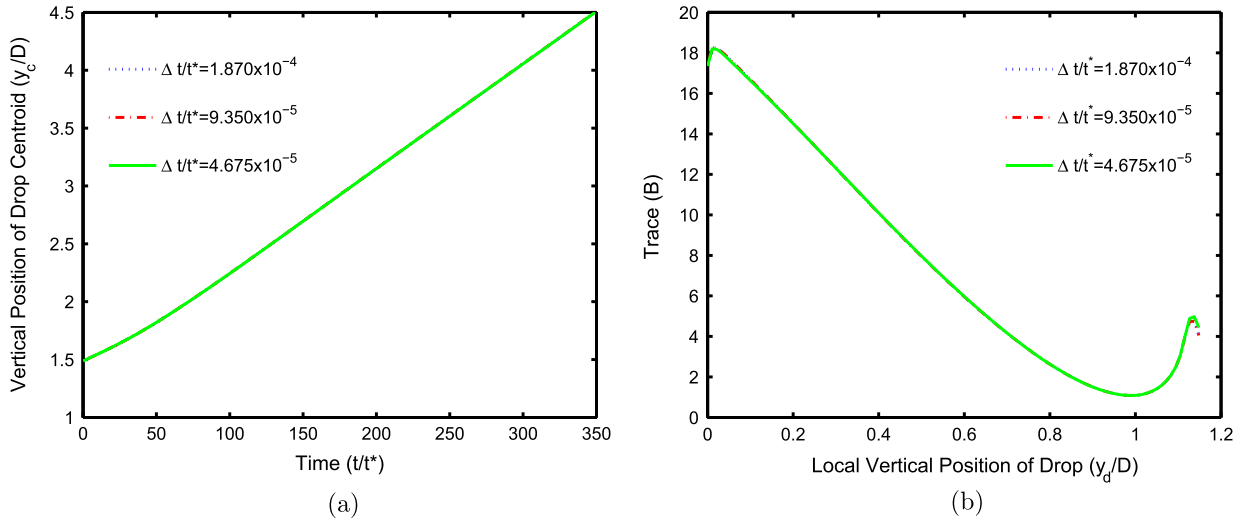

(a)

(b)

Fig. 14. Grid convergence for the VN case. (a) The terminal velocity of the droplet against the non-dimensional time. The results are obtained using $32 \times 296, 64 \times 592$ and 128×1184 grids. (b) Variation of normalized terminal velocity with the square of the non-dimensional grid size $(\Delta x/R)^2$ at $t/t^* = 40, 100$ and 160. The solid lines are the linear least squares fits to the computational results indicating the expected second-order accuracy of the method. ($Re = 10, Ca = 50, Wi = 50$).

(a)

(b)

Fig. 15. Grid convergence for the VN case. (a) Steady solution of trace(**B**) is plotted along the drop centerline. The results are obtained using various grid resolutions ranging between 16×148 and 128×1184. (b) Variation of trace(**B**) with the square of the non-dimensional grid size $(\Delta x/R)^2$ at $y_d/D = 0.2, 0.5, 1.148$. The solid lines are the linear least squares fits to the computational results indicating the expected second-order accuracy of the method. ($Ca = 50, Re = 10, Wi = 50, D = d_d$).

Fig. 16. Time-stepping error convergence for the VN case. Simulations are performed using the non-dimensional time steps $\Delta t/t^* = 1.870 \times 10^{-4}, 9.350 \times 10^{-5}$ and 4.675×10^{-5}. (a) The non-dimensional axial location of droplet centroid is plotted against the non-dimensional time. (b) The steady solution of trace($\mathbf{B}$) is plotted along the drop centerline. ($Ca = 50, Re = 10, Wi = 50, D = d_d; Grid : 64 \times 592$).
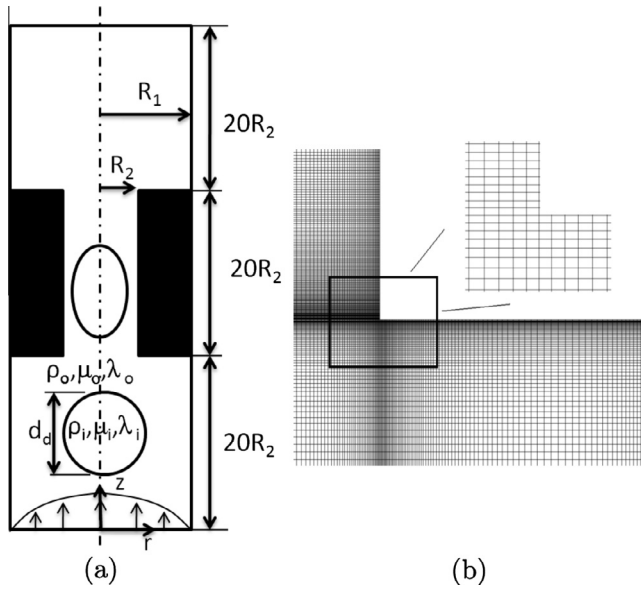

Fig. 17. (a) Schematic illustration of a pressure-driven viscoelastic two phase system. (b) Mesh near the re-entrant corner.

The physical problem is schematically shown in Fig. 17a. The flow is assumed be axisymmetric so only one half is used as the computational domain. This geometry is motivated by the recent computational studies of Chung et al. [17,18] who simulated motion of a two-dimensional viscoelastic droplet in a creeping flow through a planar constricted channel using a finite-element/front-tracking method. A similar problem has been also studied by Harvie et al. [25] who performed volume-of-fluid simulations for a viscoelastic droplet in a Newtonian fluid moving through a pressure-driven 2D planar channel with a constriction. To the best of our knowledge, the only axisymmetric simulations of a viscoelastic droplet through a constricted channel have been performed by Zhou et al. [66] as a model for neutrophil deformation and transport in capillaries. Following Chung et al. [17], the constriction ratio is selected in the present study as 5:1:5, i.e., the ratio of the tube radius to that of the constriction is $R_1/R_2 = 5$. Note that this constriction ratio is more severe in the present axisymmetric case than that in the planar flow. The tube has a total length of $60R_2$. A sudden constriction of length $20R_2$ is located at the middle of the tube as shown in Fig. 17a. A spherical droplet of diameter $d_d = 2.5R_2$ is placed instantly at the axis of the channel with a distance of $10R_2$ upwards from the inlet. A parabolic fully developed velocity profile is specified at the channel entrance
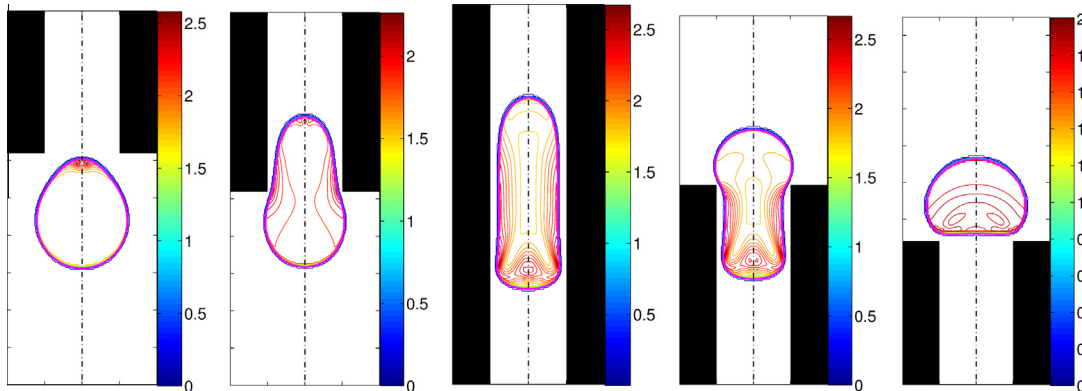

Fig. 18. An Oldroyd-B droplet moving through a Newtonian ambient fluid in a pressure driven constriction/expansion tube for $Wi = 0.4$. The constant contours represent the average polymer extension defined as $\sqrt{\text{trace}(\mathbf{A})}$. From left to right, the snapshots are taken at times $t/t^* = 0.70, 0.71, 77, 83$ and 0.85. Simulations are performed using the LCM on a 96×1152 grid ($Ca = 0.1, Re = 1$).
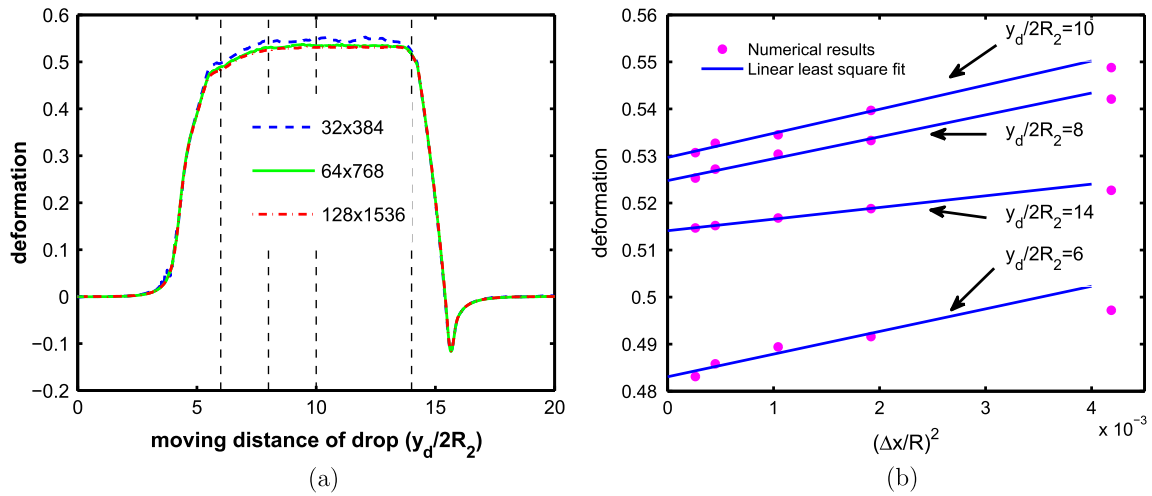
(a)   (b)

Fig. 19. Grid convergence for the VN case. The results are obtained using various grid resolutions ranging between 32×384 and 128×1536. (a) Drop deformation versus the moving distance of the drop centroid. (b) Variation of drop deformation with the square of the non-dimensional grid size $(\Delta x/R)^2$ at the axial locations $y_d/2R_2 = 6, 8, 10$ and 14. The solid lines are the linear least squares fits to the computational results indicating the expected second-order accuracy of the method. ($Wi = 0.4, Ca = 0.1, Re = 1$).
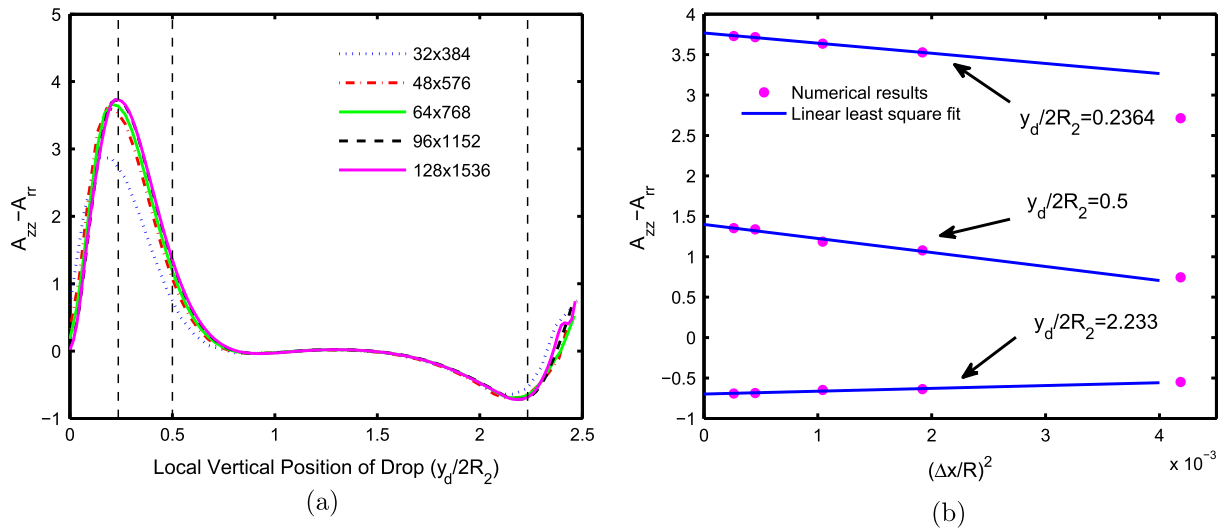

(a)   (b)

Fig. 20. Grid convergence for the VN case. The results are obtained using various grid resolutions ranging between 32×384 and 128×1536. (a) Steady distribution of $A_{zz} - A_{rr}$ along the drop centerline. (b) Variation of $A_{zz} - A_{rr}$ with the square of the non-dimensional grid size $(\Delta x/R)^2$ at the axial locations $y_d/2R_2 = 0.2364, 0.5, 2.233$. The solid lines are the linear least squares fits to the computational results indicating the expected second-order accuracy of the method. ($Wi = 0.4, Ca = 0.1, Re = 1$).
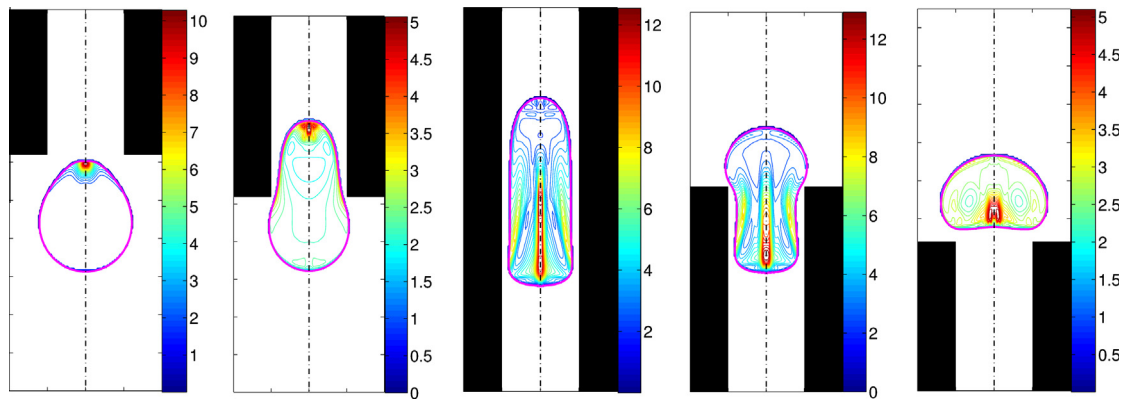

Fig. 21. An Oldroyd-B droplet moving through a Newtonian ambient fluid in a pressure driven constriction/expansion tube for $Wi = 2$. The constant contours represent the average polymer extension defined as $\sqrt{\text{trace}(\mathbf{A})}$. From left to right, the snapshots are taken at times $t/t^* = 0.70, 0.71, 77, 83$ and 0.85. Simulations are performed using the LCM on a 96×1152 grid ($Ca = 0.1, Re = 1$).
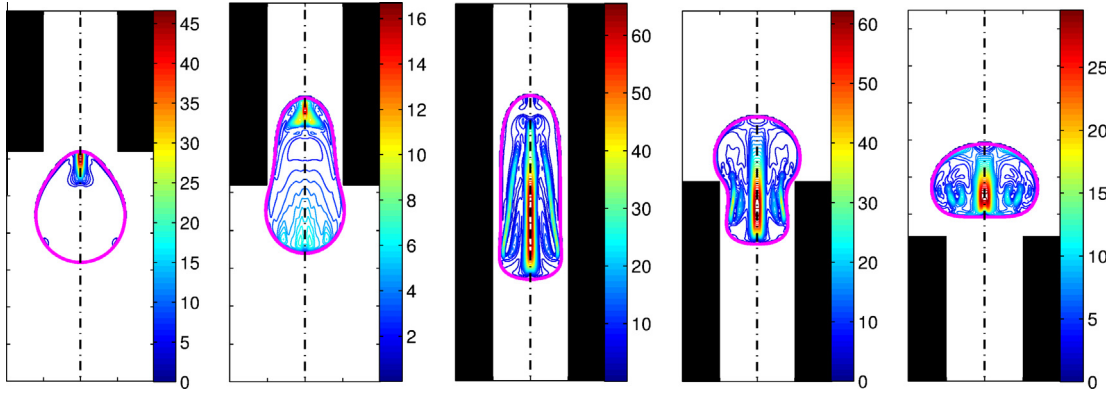
Fig. 22. An Oldroyd-B droplet moving through a Newtonian ambient fluid in a pressure driven constriction/expansion tube for $Wi = 50$. The constant contours represent the average polymer extension defined as $\sqrt{\text{trace}(\mathbf{A})}$. From left to right, the snapshots are taken at times $t/t^* = 0.70, 0.71, 77, 83$ and 0.85. Simulations are performed using the LCM on a 96×1152 grid ($Ca = 0.1, Re = 1$).
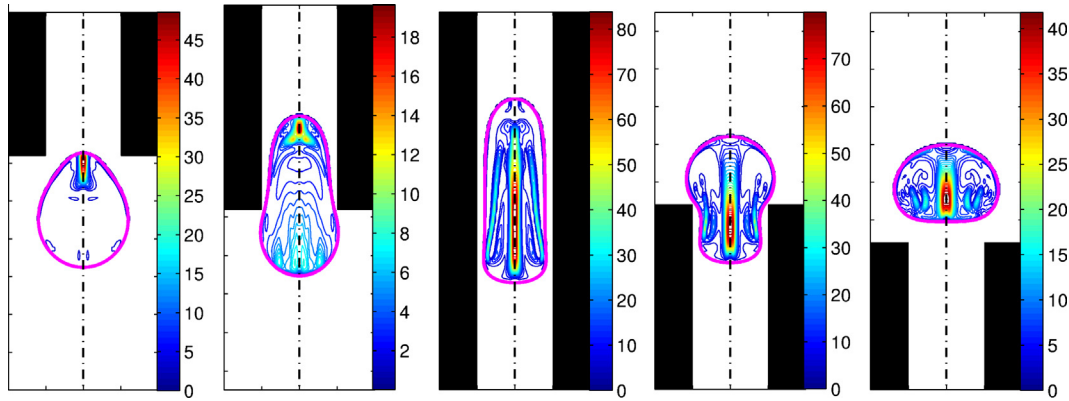

Fig. 23. An Oldroyd-B droplet moving through a Newtonian ambient fluid in a pressure driven constriction/expansion tube for $Wi = 100$. The constant contours represent the average polymer extension defined as $\sqrt{\text{trace}(\mathbf{A})}$. From left to right, the snapshots are taken at times $t/t^* = 0.70, 0.71, 77, 83$ and 0.85. Simulations are performed using the LCM on a 96×1152 grid ($Ca = 0.1, Re = 1$).
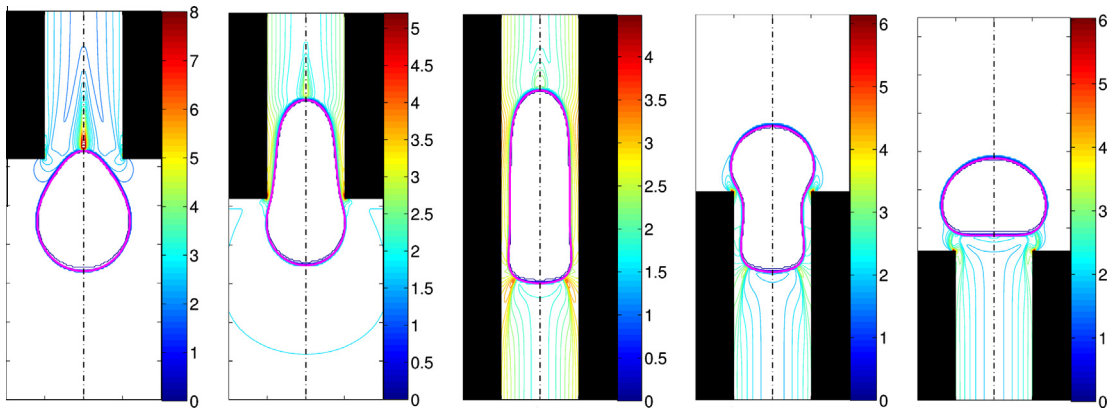

Fig. 24. A Newtonian droplet moving through an Oldroyd-B fluid in a pressure driven constriction/expansion tube for $Wi = 0.4$. The constant contours represent the average polymer extension defined as $\sqrt{\text{trace}(\mathbf{A})}$. From left to right, the snapshots are taken at times $t/t^* = 0.70, 0.71, 77, 83$ and 0.85. Simulations are performed using the LCM on a 96×1152 grid ($Ca = 0.1, Re = 1$).

and the pressure is fixed at the exit. The viscoelastic stresses are specified at the inlet based on the analytical solution assuming a fully developed pipe flow, i.e.,

$$\tau_{rr} = 0; \quad \tau_{\theta\theta} = 0; \quad \tau_{rz} = \mu_p \frac{\partial v_z}{\partial r}; \quad \tau_{zz} = 2\lambda\tau_{rz}\frac{\partial v_z}{\partial r}. \tag{18}$$

The Neumann boundary conditions are applied at the other boundaries.

In addition to the property ratios defined in Eq. (17), the relevant dimensionless parameters are the capillary (Ca), the Weissenberg (Wi) and the Reynolds (Re) numbers defined as

$$Ca = \frac{\mu_o U}{\sigma}; \quad Wi = \frac{\lambda U}{R_2}; \quad Re = \frac{\rho_o U R_2}{\mu_o}, \tag{19}$$

where U is the mean velocity in the narrow part of the tube. Drop deformation is defined as

$$\text{deformation} = \frac{W_b - H_b}{W_b + H_b}, \tag{20}$$

where W_b and H_b are the maximum droplet dimensions in the axial and radial directions, respectively. The capillary number, the Reynolds number and the property ratios are fixed at $Ca = 0.1, Re = 1, \beta = 0.5, \theta = 0.5$ and $\alpha = 1.17$ in all the results presented in this section. The computations are again performed using dimensional quantities but the results are made dimensionless using the length scale R_2 and time scale $t^* = 125 R_2/U$.

The simulations are first performed for the dimensionless numbers that are of the same order of those in Chung et al. [17,18]. The computational grid is stretched near the walls and in the vicinity of the constriction similar to the single-phase flow case (Fig. 17b). The semi-analytical method is found to be convergent only up to $Wi = 2$ for the Oldroyd-B fluid model for this flow. Thus computations are performed using the log-conformation in all the results presented in this section. Figs. 18 and 21 show the evolution of an Oldroyd-B droplet moving in a Newtonian fluid (VN system) through the constriction for $Wi = 0.4$ and $Wi = 2$, respectively.

Before presenting further results, a comprehensive study is conducted to demonstrate the grid convergence and determine the appropriate grid resolution for this pressure-driven case. Sample results are presented here for the VN system only. For this purpose, simulations are performed for the VN system shown in Fig. 18 using various grid resolutions ranging between 32×384 and 128×1536. The evolution of drop deformation and the steady solution of $A_{zz} - A_{rr}$ along the drop centerline are plotted in Figs. 19a and 20a, respectively. As can be seen in these figures, differences between successive grid resolutions decrease as grid is refined indicating grid convergence. To quantify the spatial error, values of drop deformation and $A_{zz} - A_{rr}$ are plotted at selected locations against the square of non-dimensional grid size in Figs. 19b and 20b, respectively. The approximate linear relationship confirms the expected second order spatial accuracy of the method. These figures show that a 96×1152 grid is required to reduce the maximum spatial error below 4% for $A_{zz} - A_{rr}$ while only a 64×768 grid is sufficient to reduce the spatial error below 1% in the drop deformation. Note that the results presented in this paper are obtained using a 96×1152 grid for which the maximum spatial error is reduced below 4% in all the flow quantities.

In order to demonstrate the robustness of the numerical method, simulations are also performed for much higher Weissenberg numbers and sample results are plotted in Figs. 22 and 23 for $Wi = 50$ and $Wi = 100$, respectively. The constant contours of $\sqrt{\text{trace}(\mathbf{A})}$ are used to quantify the evolution of the viscoelastic stresses. It is seen that, as the leading tip of the drop enters the contraction, the region in the vicinity of the front stagnation point contains significantly extended polymers due to extensional flow leading to accumulation of viscoelastic stresses there. As the droplet further progresses into the constriction, significant stress concentration also occurs on the side of the droplet due to high shear stresses exerted by the ambient fluid near the wall. These viscoelastic stresses are then convected toward the
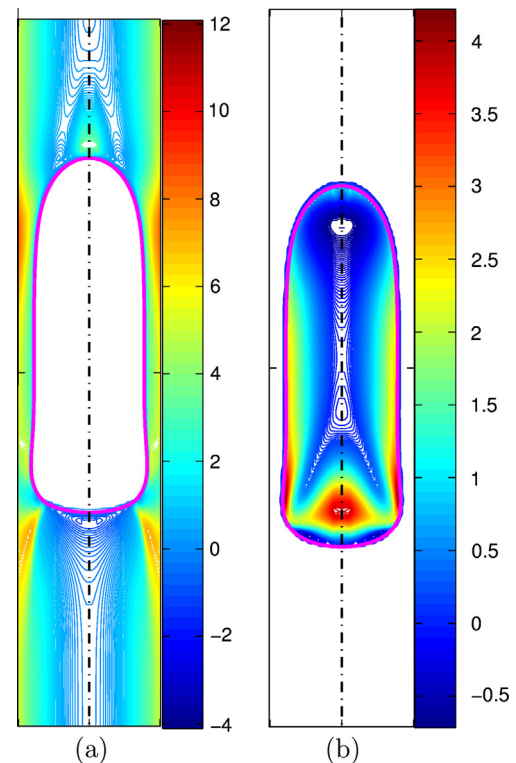

(a)   (b)

Fig. 26. The constant contours of the difference between the normal components of the conformation tensor $A_{zz} - A_{rr}$ in the vicinity of the droplet in the constriction. (a) NV system and (b) VN system. ($Ca = 0.1, Re = 1, Wi = 0.4$ and $Grid : 96 \times 1152$.)
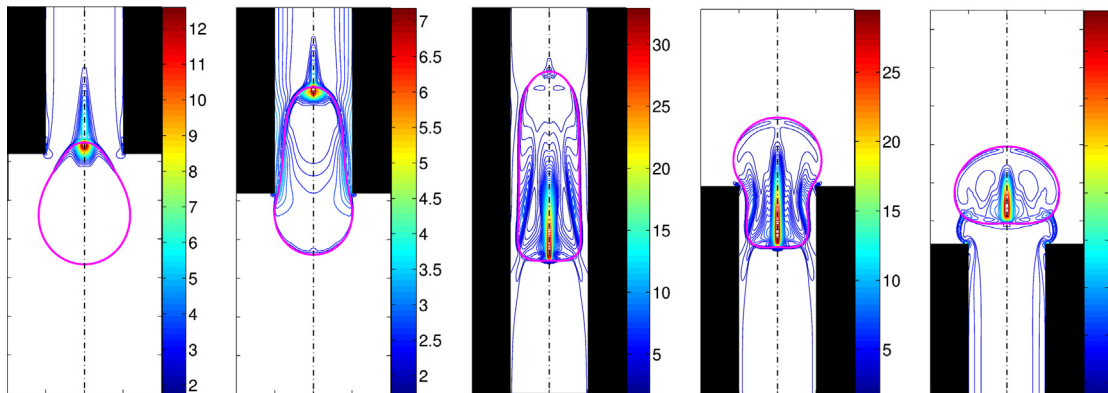

Fig. 25. An Oldroyd-B droplet moving through another Oldroyd-B fluid in a pressure-driven constriction/expansion tube for $Wi_i = 2$ and $Wi_o = 0.4$. The constant contours represent the average polymer extension defined as $\sqrt{\text{trace}(\mathbf{A})}$. From left to right, the snapshots are taken at times $t/t^* = 0.70, 0.71, 77, 83$ and 0.85. Simulations are performed using the LCM on a 96×1152 grid ($Ca = 0.1, Re = 1$).

trailing edge mainly by the internal circulation and accumulated near the centerline when the droplet reaches a nearly steady motion in the constriction. As droplet leaves the constriction, the fluid decelerates resulting in negative extensional strain that reduces droplet length forming a part-moon shape. The droplet eventually relaxes to a nearly spherical shape due to surface tension. The stress patterns are similar for all Weissenberg number cases but the viscoelastic effects are more pronounced as *Wi* increases. Similar simulations are also performed for a Newtonian droplet in a viscoelastic medium (NV) and a viscoelastic droplet in another viscoelastic medium (VV). Figs. 24 and 25 show the evolution of the NV and VV systems, respectively. Similar to the VN case, in the NV system, the viscoelastic stresses concentrate near the leading edge as drop enters the constriction and then move toward the side of the droplet near the tube wall mainly due to the shear stresses exerted by the ambient fluid. In the case of VV, the stress patterns are a combination of the VN and NV cases. The constant contours of $A_{zz} - A_{rr}$ are plotted in Fig. 26 both for the VN and NV cases in the middle of constriction when the

droplet reaches a nearly steady motion. For the VN case, the normal stress differences develop inside the drop on the sides close to the wall as well as near the rear stagnation point. For the NV case, the normal stress differences are significantly higher in the film region as seen in Fig. 26a. In the both cases, the high stress difference on the sides helps the drop swell at the exit of the constriction since the normal stress difference exerts force in the radial direction.

Typical deformation patterns are illustrated in Fig. 27a for the all Newtonian case (NN), i.e., $Wi = 0$. The deformation is plotted against the moving distance y_d defined as the distance that the droplet travels in the axial direction relative to its initial position. For the same case, the deformations in the axial and radial directions are plotted separately in Fig. 27b. The drop deforms as it moves into the constriction and becomes more elongated due to increased confinement. Once the centroid of the drop is within the capillary its rear is held by the contraction while its front continues to elongate. After some time the rear of the drop clears the contraction and drop attains a nearly steady shape in the narrow channel. As
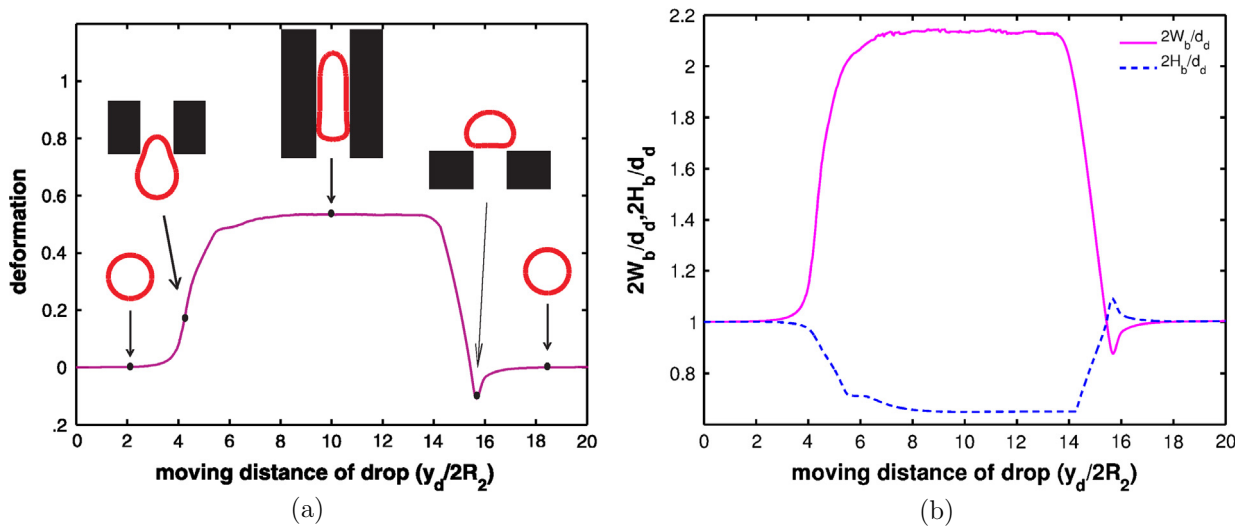

Fig. 27. Drop deformation versus the moving distance of the drop centroid for the Newtonian-Newtonian system (NN). (a) The drop deformation and the corresponding drop shapes. (b) The drop deformation in the axial (solid line) and the radial (dashed line) directions, respectively. ($Wi = 0, Re = 1, Ca = 0.1$ and $Grid : 96 \times 1152$.)

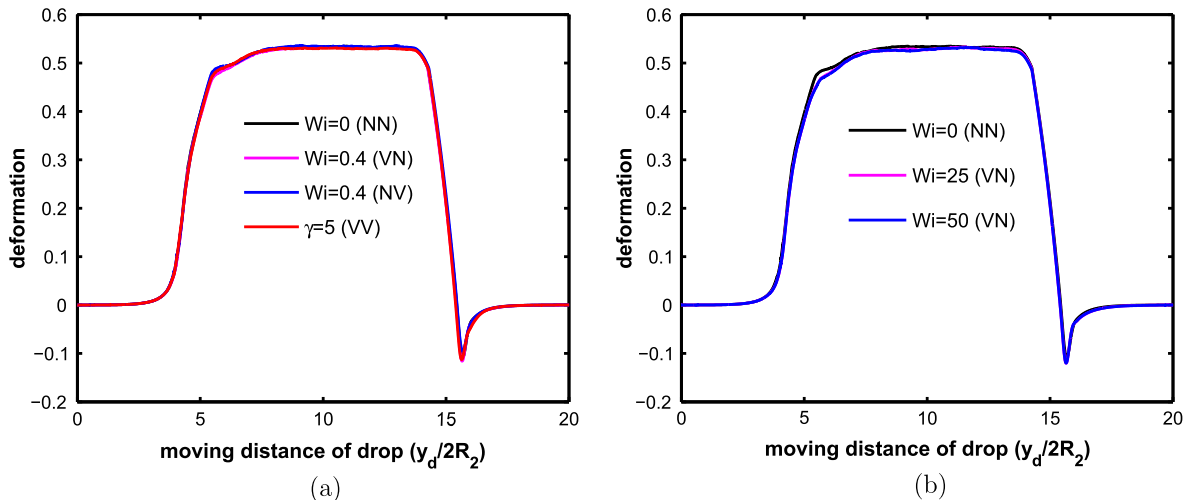**Fig. 28.** Effects of fluid elasticity on drop deformation. The simulations are performed using a 96×1152 grid for $Re = 1$ and $Ca = 0.1$. (a) Oldroyd-B model ($Wi_i = 2, Wi_o = 0.4$ for VV), (b) FENE-CR model ($L = 5$).
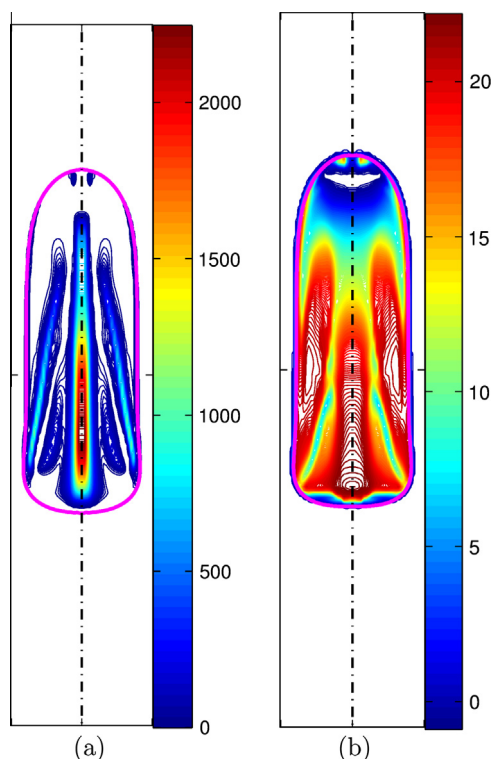
Fig. 29. The constant contours of $A_{zz} - 1$ for a viscoelastic drop in a Newtonian fluid for $Wi = 25, Re = 1, Ca = 0.1$. The simulations are performed on a 96×1152 grid. (a) Oldroyd-B model. (b) FENE-CR model ($L = 5$).

drop leaves the constriction, it swells as indicated by the negative deformation in Fig. 27a. Finally, the droplet restores its spherical shape due to surface tension in the expansion region. Drop deformation is compared in Fig. 28 for NV, VN and VV cases both for the Oldroyd-B and FENE-CR models. As can be seen in this figure, the drop deformation is almost identical for NV, VN and VV systems irrespective of the elastic properties of the fluids. Note that the present results are qualitatively similar to the 2D planar simulations of Chung et al. [18].

Finally simulations are performed for a high Weissenberg number case, i.e., $Wi = 25$, to demonstrate the difference between the Oldroyd-B and FENE-CR models. The results are shown in Fig. 29 where the constant contours of $A_{zz} - 1$ are plotted both for the Oldroyd-B and FENE-CR models. As can be seen, the Oldroyd-B model results in a large build up of polymer extensions along the droplet centerline (Fig. 29a) whereas the polymer extension is moderate in the FENE-CR model case (Fig. 29b). This is a direct result of the finitely extensible nature of the FENE-CR model and is the main reason that the Oldroyd-B model presents a considerable challenge to numerical simulations especially at high Weissenberg numbers. The present results demonstrate that the front-tracking method is robust and successfully simulates viscoelastic two-phase systems at high Weisenberg numbers, i.e., as high as $Wi = 100$ for Oldroyd-B model.

5. Conclusions

A front-tracking method is developed for direct numerical simulations of viscoelastic interfacial flows. The method is general and applicable to two-phase systems in which either phase or both phases can be viscoelastic. It can accommodate virtually any viscoelastic model for each phase. Moreover, the method is readily extendible for simulation of multiphase systems in which more than two-phases may exist.

Semi-analytical and log-conformation schemes are used to integrate the viscoelastic constitutive equations in time. The log-conformation method is found to be in good agreement with the semi-analytical method and very robust for a wide range of Weissenberg numbers. A fifth-order upwinded WENO-Z scheme is used to discretize the convective terms in the viscoelastic model equations and found to be crucially important for resolving thin viscoleastic boundary layers near the interface.

The method is first validated for single-phase viscoelastic flows including a start up flow in a circular channel and a pressure-driven flow through a 4:1 constriction. Then it is applied to buoyancy-driven motion of viscoelastic two-phase systems encompassing a viscoelastic droplet in Newtonian medium, a Newtonian droplet in a viscoelastic medium and a viscoelastic droplet in another viscoelastic medium. The results are compared and found to be in good qualitative and quantitative agreement with the computational simulations of You et al. [64]. Moreover, the present method is found to be stable and very robust for very low solvent viscosity ratios, i.e., as low as $\beta = 10^{-4}$. It is also verified that the results obtained using the log-conformation and semi-analytical methods are consistent. Finally, the method is applied to study the dynamics of viscoelastic droplet systems in a pressure-driven contraction/expansion channel. It is found that the log-conformation method is stable and preserves positive definiteness of conformation tensor for a wide range of Weissenberg numbers whereas the semi-analytical method remains stable only for small or moderate Weissenberg numbers, i.e., up to $Wi = 2$ for this case. However the semi-analytical method has advantage of requiring lower computational time and implementation complexity compared to the log-conformation method. Thus the semi-analytical method is an optimal choice for computation of viscoleastic flows at small or moderate Weissenberg numbers. It is also worth to note that the log-conformation method can provide stable simulations at large Weissenberg numbers, but it cannot guarantee accuracy at arbitrarily high Weissenberg numbers as discussed by Fattal and Kupferman [20].

Acknowledgement

References

[1] N. Aggarwal, K. Sarkar, Deformation and breakup of a viscoelastic drop in a Newtonian matrix under steady shear, J. Fluid Mech. 584 (2007) 1–21.
[2] L.J. Amoreira, P.J. Oliveira, Comparison of different formulations for the numerical calculation of unsteady incompressible viscoelastic fluid flow, Adv. Appl. Math. Mech. 2 (4) (2010) 483–502.
[3] M.G.H.M. Baltussen, M.A. Hulsen, G.W.M. Peters, Numerical simulation of the fountain flow instability in injection molding, J. Non-Newtonian Fluid Mech. 165 (2010) 631–640.
[4] A.N. Beris, K.D. Housiadas, Computational viscoelastic fluid mechanics and numerical studies of turbulent flows of dilute polymer solutions, in: P.D. Gujrati, A.I. Leonov (Eds.), Modeling and Simulation in Polymers, Wiley-VCH Verlag, Weinheim, Germany, 2010. doi: http://dx.doi.org/10.1002/9783527630257.ch1.
[5] R.B. Bird, P.J. Dotson, N.L. Johnson, Polymer solution rheology based on a finitely extensible bead-spring chain model, J. Non-Newtonian Fluid Mech. 7 (1980) 213–235.
[6] A. Bonito, M. Picasso, M. Laso, Numerical simulation of 3D viscoelastic flows with free surfaces, J. Comput. Phys. 215 (2006) 691–716.
[7] R. Borges, M. Carmona, B. Costa, W.S. Don, An improved weighted essentially non-oscillatory scheme for hyperbolic conservation laws, J. Comput. Phys. 227 (2008) 3191–3211.
[8] D. Borzacchiello, E. Leriche, B. Blottiere, J. Guillet, Three-dimensional finite volume computation of viscoelastic fluid encapsulation by phase-field modeling, J. Non-Newtonian Fluid Mech. 200 (2013) 52–64.

[9] D.W. Bousfield, R. Keunings, G. Marruci, M.M. Denn, Non-linear analysis of the surface tension driven breakup of viscoelastic filaments, J. Non-Newtonian Fluid Mech. 21 (1986) 79–97.

[10] D.W. Bousfield, R. Keunings, M.M. Denn, Transient deformation of an inviscid inclusion in a viscoelastic extensional flow, J. Non-Newtonian Fluid Mech. 27 (1988) 205–221.

[11] P.J. Coates, R.C. Armstrong, R.A. Brown, Calculation of steady-state viscoelastic flow through axisymmetric contractions with the EEME formulation, J. Non-Newtonian Fluid Mech. 42 (1992) 141–188.

[12] X. Chen, H. Marshall, M. Schafer, D. Bothe, A comparison of stabilisation approaches for finite-volume simulation of viscoelastic fluid flow, Int. J. Comput. Fluid Dyn. 27 (6–7) (2013) 229–250.

[13] M.D. Chilcott, J.M. Rallison, Creeping flow of dilute polymer solutions past cylinders and spheres, J. Non-Newtonian Fluid Mech. 29 (1988) 381–432.

[14] T. Chinyoka, Y.Y. Renardy, M. Renardy, D.B. Khismatullin, Two-dimensional study of drop deformation under simple shear for Oldroyd-B liquids, J. Non-Newtonian Fluid Mech. 130 (2005) 45–56.

[15] Y.J. Choi, M.A. Hulsen, Simulation of extrudate swell using an extended finite element method, Korea-Aust. Rheol. J. 23 (2011) 147–154.

[16] A.R. Chorin, Numerical solution of the Navier–Stokes equations, Math. Comput. 22 (1968) 745–762.

[17] C. Chung, M.A. Hulsen, J.M. Kim, K.H. Ahn, S.J. Lee, Numerical study on the effect of viscoelasticity on drop deformation in simple shear and 5:1:5 planar contraction/expansion microchannel, J. Non-Newtonian Fluid Mech. 155 (2008) 80–93.

[18] C. Chung, J.M. Kim, M.A. Hulsen, K.H. Ahn, S.J. Lee, Effect of viscoelasticity on drop dynamics in 5:1:5 planar contraction/expansion microchannel flow, Chem. Eng. Sci. 64 (2009) 4515–4524.

[19] M.J. Crochet, R. Keunings, Finite element analysis of die-swell of highly elastic fluid, J. Non-Newtonian Fluid Mech. 10 (1982) 339–356.

[20] R. Fattal, R. Kupferman, Time-dependent simulation of viscoelastic flows at high Weissenberg number using the log-conformation representation, J. Non-Newtonian Fluid Mech. 126 (2005) 23–37.

[21] M. Furuichi, M. Kameyama, A. Kageyama, Three-dimensional Eulerian method for large deformation of viscoelastic fluid: toward plate-mantle simulation, J. Comput. Phys. 227 (2008) 4977–4997.

[22] H. Giesekus, A simple constitutive equation for polymer fluids based on the concept of deformation-dependent tensorial mobility, J. Non-Newtonian Fluid Mech. 11 (1982) 69–109.

[23] F. Habla, H. Marschall, O. Hinrichsen, L. Dietsche, H. Jasak, J.L. Favero, Numerical simulation of viscoelastic two-phase flows using openFOAM, Chem. Eng. Sci. 66 (2011) 5487–5496.

[24] A. Harten, High resolution schemes for hyperbolic conservation laws, J. Comput. Phys. 49 (1983) 357–393.

[25] D.J.E. Harvie, J.J. Cooper-White, M.R. Davidson, Deformation of a viscoelastic droplet passing through a microfluidic contraction, J. Non-Newtonian Fluid Mech. 155 (2008) 67–79.

[26] M.A. Hulsen, A sufficient condition for a positive definite configuration tensor in differential models, J. Non-Newtonian Fluid Mech. 38 (1) (1990) 93–100.

[27] M.A. Hulsen, R. Fattal, R. Kupferman, Flow of viscoelastic fluids past a cylinder at high Weissenberg number: stabilized simulations using matrix logarithms, J. Non-Newtonian Fluid Mech. 127 (2005) 27–39.

[28] R. Keunings, An algorithm for the simulation of transient viscoelastic flows with free surfaces, J. Comput. Phys. 62 (1986) 199–220.

[29] M.I. Kolte, H.K. Rasmussen, O. Hassager, Transient filament stretching rheometer. 2. Numerical simulation, Rheol. Acta 36 (1997) 285–302.

[30] S.J. Lind, T.N. Phillips, The effects of viscoelasticity on a rising gas bubble, J. Non-Newtonian Fluid Mech. 165 (2010) 852–865.

[31] J.M. Marchal, M.G. Crochet, A new mixed finite element for calculating viscoelastic flow, J. Non-Newtonian Fluid Mech. 26 (1987) 77–144.

[32] G. Mompean, M. Deville, Unsteady finite volume of Oldroyd-B fluid through a three-dimensional planar contraction, J. Non-Newtonian Fluid Mech. 72 (1997) 253–279.

[33] S. Mukherjee, K. Sarkar, Effects of viscoelasticity on the retraction of a sheared drop, J. Non-Newtonian Fluid Mech. 165 (2010) 340–349.

[34] S. Mukherjee, K. Sarkar, Viscoelastic drop falling through a viscous medium, Phys. Fluids 23 (2011) 013101.

[35] S. Mukherjee, K. Sarkar, Effects of matrix viscoelasticity on the lateral migration of a deformable drop in wall-bounded shear, J. Fluid Mech. 727 (2013) 318–345.

[36] M. Muradoglu, A.D. Kayaalp, An auxiliary grid method for computations of multiphase flows in complex geometries, J. Comput. Phys. 214 (2006) 858–877.

[37] M. Muradoglu, H.A. Stone, Motion of large bubbles in curved channels, J. Fluid Mech. 570 (2007) 455–466.

[38] M. Muradoglu, G. Tryggvason, Simulations of soluble surfactants in 3D multiphase flow, J. Comput. Phys. 274 (2014) 737–757.

[39] C.M. Oishi, F.P. Martins, M.F. Tome, M.A. Alves, Numerical simulation of drop impact and jet buckling problems using the eXtended Pom-Pom model, J. Non-Newtonian Fluid Mech. 169–170 (2012) 91–103.

[40] J.G. Oldroyd, On the formulation of rheological equations of state, Proc. R. Soc. Lond. A 200 (1950) 523–541.

[41] U. Olgac, M. Muradoglu, Computational modeling of unsteady surfactant-laden liquid plug propagation in neonatal airways, Phys. Fluids 25 (7) (2013). Art. No. 071901.

[42] R.G. Owens, T.N. Phillips, Computational Rheology, Imperial College Press, London, UK, 2002.

[43] G.S. Paulo, C.M. Oishi, M.F. Tome, M.A. Alves, F.T. Pinho, Numerical solution of the FENE-CR model in complex flows, J. Non-Newtonian Fluid Mech. 204 (2014) 50–61.

[44] C. Peskin, Numerical analysis of blood flow in the hearth, J. Comput. Phys. 25 (1977) 220–252.

[45] S.B. Pillapakkam, P. Singh, A level-set method for computing solutions to viscoelastic two-phase flow, J. Comput. Phys. 174 (2001) 552–578.

[46] S.B. Pillapakkam, P. Singh, D. Blackmore, N. Aubry, Transient and steady state of a rising bubble in a viscoelastic fluid, J. Fluid Mech. 589 (2007) 215–252, http://dx.doi.org/10.1017/S0022112007007628.

[47] S. Ramaswamy, L.G. Leal, The deformation of a viscoelastic drop subjected to steady uniaxial extensional flow of a Newtonian fluid, J. Non-Newtonian Fluid Mech. 85 (1999) 27–163.

[48] K. Sarkar, W.R. Schowalter, Deformation of a two-dimensional viscoelastic drop at non-zero Reynolds number in time-periodic extensional flows, J. Non-Newtonian Fluid Mech. 95 (2000) 315–342.

[49] T.M. Squires, S.R. Quake, Microfluidics: fluid physics at the nanoliter scale, Rev. Mod. Phys. 77 (3) (2005) 977–1026.

[50] R.I. Tanner, A theory of die-swell, J. Polym. Sci. 8 (1970) 2067–2078.

[51] R.I. Tanner, Engineering Rheology, Oxford University Press, Oxford, Clarendon, UK, 2000.

[52] S. Tasoglu, G. Kaynak, A.J. Szeri, U. Demirci, M. Muradoglu, Impact of a compound droplet on a flat surface: a model for single cell epitaxy, Phys. Fluids 22 (2010) 082103.

[53] M.F. Tome, L. Grossi, A. Castelo, J.A. Cuminato, S. McKee, K. Walters, Die-swell, splashing drop and a numerical technique for solving the Oldroyd-B model for axisymmetric free surface flows, J. Non-Newtonian Fluid Mech. 141 (2007) 148–166.

[54] M.F. Tome, A. Castelo, A.M. Afonso, M.A. Alves, F.T. Pinho, Application of the log-conformation tensor to three-dimensional time-dependent free surface flows, J. Non-Newtonian Fluid Mech. 175–176 (2012) 44–54.

[55] G. Tryggvason, B. Bunner, A. Esmaeeli, D. Juric, N. Al-Rawahi, W. Tauber, J. Han, S. Nas, Y.-J. Jan, A front-tracking method for the computations of multiphase flow, J. Comput. Phys. 169 (2) (2001) 708–759.

[56] G. Tryggvason, R. Scardovelli, S. Zaleski, Direct Numerical Simulations of Gas–Liquid Multiphase Flows, Cambridge University Press, Cambridge, UK, 2011.

[57] S.O. Unverdi, G. Tryggvason, A front-tracking method for viscous, incompressible, multi-fluid flows, J. Comput. Phys. 100 (1) (1992) 25–37.

[58] C. Verdier, C. Couzon, A. Duperray, P. Singh, Modeling cell interactions under flow, J. Math. Biol. 58 (2009) 235–259.

[59] M.M. Villone, M.A. Hulsen, P.D. Anderson, P.L. Maffettone, Simulations of deformable systems in fluids under shear flow using an arbitrary Lagrangian Eulerian technique, Comput. Fluids 90 (2014) 88–100.

[60] N.D. Waters, M.J. King, The unsteady flow of an elastico-viscous liquid in a straight pipe of circular cross section, J. Phys. D: Appl. Phys. 4 (1971) 204–211.

[61] X. Xu, J. Ouyang, A SPH-based particle method for simulating 3D transient free surface flows of branched polymer melts, J. Non-Newtonian Fluid Mech. 202 (2013) 54–71.

[62] P. Yue, C. Zhou, J.J. Feng, C.F. Ollivier-Gooch, H.H. Hu, Phase-field simulations of interfacial dynamics in viscoelastic fluids using finite elements with adaptive meshing, J. Comput. Phys. 219 (2006) 47–67.

[63] R. You, A. Borhan, H. Haj-Hariri, A finite volume formulation for simulating drop motion in a viscoelastic two-phase system, J. Non-Newtonian Fluid Mech. 153 (2008) 09–129.

[64] R. You, H. Haj-Hariri, A. Borhan, Confined drop motion in viscoelastic two-phase systems, Phys. Fluids 21 (2009). Art. No. 013102.

[65] C. Zhou, P. Yue, J.J. Feng, Formation of simple and compound drops in microfluidic devices, Phys. Fluids 18 (2006) 092105.

[66] C. Zhou, P. Yue, J.J. Feng, Simulation of neutrophil deformation and transport in capillaries using Newtonian and viscoelastic drop models, Ann. Biomed. Eng. 35 (2007) 766–780.

[67] C. Zhou, P. Yue, J.J. Feng, C.F. Ollivier-Gooch, H.H. Hu, 3D phase-field simulations of interfacial dynamics in Newtonian and viscoelastic fluids, J. Comput. Phys. 229 (2010) 498–511.